

Accepted Manuscript

Title: Mn-Schiff base modified MCM-41, SBA-15 and CMK-3 NPs as Single-Site Heterogeneous catalysts: Alkene Epoxidation with H₂O₂ incorporation

Author: A. Mavrogiorgou M. Baikousi V. Costas E. Mouzourakis Y. Deligiannakis M.A. Karakassides M. Louloudi



PII: S1381-1169(15)30178-3
DOI: <http://dx.doi.org/doi:10.1016/j.molcata.2015.12.015>
Reference: MOLCAA 9717

To appear in: *Journal of Molecular Catalysis A: Chemical*

Received date: 8-10-2015
Revised date: 15-12-2015
Accepted date: 21-12-2015

Please cite this article as: A.Mavrogiorgou, M.Baikousi, V.Costas, E.Mouzourakis, Y.Deligiannakis, M.A.Karakassides, M.Louloudi, Mn-Schiff base modified MCM-41, SBA-15 and CMK-3 NPs as Single-Site Heterogeneous catalysts: Alkene Epoxidation with H₂O₂ incorporation, *Journal of Molecular Catalysis A: Chemical* <http://dx.doi.org/10.1016/j.molcata.2015.12.015>

This is a PDF file of an unedited manuscript that has been accepted for publication. As a service to our customers we are providing this early version of the manuscript. The manuscript will undergo copyediting, typesetting, and review of the resulting proof before it is published in its final form. Please note that during the production process errors may be discovered which could affect the content, and all legal disclaimers that apply to the journal pertain.

**Mn-Schiff base modified MCM-41, SBA-15 and CMK-3 NPs as
Single-Site Heterogeneous catalysts: Alkene Epoxidation with
H₂O₂ incorporation**

**A. Mavrogiorgou^a, M. Baikousi^b, V. Costas^b, E. Mouzourakis^c, Y. Deligiannakis^c, M.
A. Karakassides^b and M. Louloudi^{a*}**

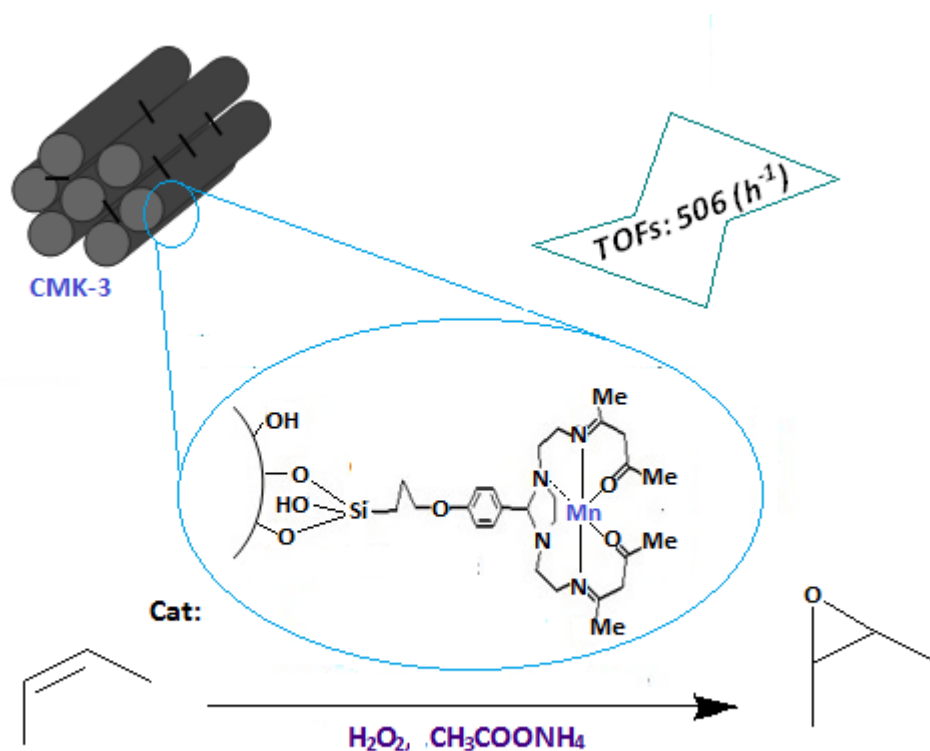
^a Department of Chemistry, University of Ioannina, 45110 Ioannina, Greece

^b Department of Materials Science and Engineering, University of Ioannina, 45110
Ioannina, Greece

^c Physics Department, University of Ioannina, 45110 Ioannina, Greece

e-mail: mlouloud@uoi.gr

Graphical abstract



Highlights

- Mn-catalysts were synthesized by covalent grafting onto SBA-15, MCM-41 and CMK-3.
- These catalysts are effective and selective towards epoxides with H_2O_2 and $\text{CH}_3\text{COONH}_4$.
- **Mn^{II}-L@CMK-3** provides high TONs and is kinetically very fast demonstrating extremely high TOFs.

Abstract

The development of new functional catalytic materials prepared via appropriate chemical modification of mesoporous silica SBA-15, MCM-41 or carbon nanomaterials CMK-3 are presented. Their synthesis has been carried out via two synthetic approaches: a) a *two steps procedure* which includes grafting of the Schiff base ligand 1,3-bis[3-aza-3-(1-methyl-3-oxobut-1-enyl)-prop-3-en-1-yl]-2-(4-hydroxy-phenyl)-1,3-imidazolidine (**L**) onto the supports and subsequent metalation of the so-formed hybrid material, and b) an *one step procedure* which allows covalent grafting of the entire [Mn^{II}-Schiff base] catalyst onto the carbonaceous support. The resulting single-site heterogeneous catalysts were characterized and evaluated for alkene epoxidation with H₂O₂ in the presence of CH₃COONH₄ as additive. They are effective and selective towards formation of epoxides. The highest TONs have been achieved by **L@MCM-41-Mn^{II}** and **Mn^{II}-L@CMK-3**. Moreover, **Mn^{II}-L@CMK-3** is operative for a second use and kinetically very fast, demonstrating remarkably high TOFs 65-634 h⁻¹ that is correlated to its practically zero porosity. Based on the present data, the textural features of the obtained catalysts are discussed in correlation with their catalytic performance.

Keywords: catalytic epoxidation; supported manganese complexes; H₂O₂ activation; mesoporous MCM-41, SBA-15, CMK-3

1. Introduction

During previous decade, the replacement of stoichiometric and homogeneous oxidation processes by environmentally friendly technologies which employ i) heterogeneous catalysts and ii) “green” oxidants, e.g. such as H_2O_2 , has become a widely accepted strategy. Rational design for effective and selective heterogeneous catalysts requires well defined spatially-separated active sites i.e. as in conventional homogeneous systems, and easy separation, recover and recyclability, as offered by heterogeneous systems [1]. The development of ‘single-site heterogeneous catalysts’ can be achieved by heterogenization of homogeneous single-site catalysts on mesoporous inorganic solids, combining by this way the advantages of both molecular/homogeneous catalysts and heterogeneous ones [2-6]. In catalytic oxidation reactions, when “green” oxidants are concerned, hydrogen peroxide, which is probably the best terminal oxidant -after dioxygen- is highly desirable i.e. taking into account both environmental and economic considerations [7]. Within this context, it has been demonstrated that alkene epoxidation by hydrogen peroxide catalyzed by cheap, ‘single-site heterogeneous catalysts’ is potentially promising for applications in chemical process and for large scale production of epoxides [3,7].

The goals of the present study are i) the development of ‘single-site heterogeneous catalysts’ by covalently grafting of $[\text{Mn}^{\text{II}}\text{-Schiff base}]$ complexes onto mesoporous nanomaterials MCM-41, SBA-15 and CMK-3 and ii) the evaluation of these hybrid organic-inorganic catalysts in alkenes’ oxidation with H_2O_2 . Among evaluation criteria for the developed catalysts are catalyst’s efficiency, i.e. high substrate conversions, high epoxide yields, high TONs, recovery and re-usability. For successful ‘single-site heterogeneous catalysts’, key-parameters should comprise optimal synthetic heterogenization process and appropriate textural/chemical features of the used inorganic supports, i.e., surface area, porosity, polarity or hydrophobicity [3-6].

In this context, MCM-41 exhibits high specific surface area ($\sim 1000 \text{ m}^2/\text{g}$), high crystallinity, high thermal stability, uniformity of hexagonal cylindrical pores, narrow pore distribution and regulated pore diameter from 15 to 100 \AA [8]. SBA-15 with its hexagonal 2D-porous structure of almost uniform cylindrical mesopores and supplementary micropores, located into the amorphous silica walls, exhibits high surface

area ($\sim 700 \text{ m}^2/\text{g}$) and tunable large uniform pore sizes ($\sim 100 \text{ \AA}$) [9]. Ordered mesoporous carbon CMK-3 is a unique porous carbonaceous material that possess a well-ordered hexagonal structure composed from uniformly sized carbon nanorods, with large surface area ($\sim 1520 \text{ m}^2/\text{g}$) and high specific pore volume, along with tunable pore size ($\sim 70 \text{ \AA}$) [10,11]. CMK-3 can be synthesized by applying the mesoporous silica sieve SBA-15 as a template and sucrose as the carbon source [12,13]; it has gained considerable interest as new nanoscaffold due to its potential applications as adsorbent, catalyst support and material for advanced electronics applications [14-19].

In the front of development of alkene epoxidation catalysts, so far few studies have been reported for covalently grafting of Schiff base metal-complexes onto mesoporous MCM-41 [20-28], SBA-15 [29,30] and CMK-3 [31]. In these cases, the main adopted synthetic strategy involved Schiff base immobilization via reaction with the surface modified silicon-based materials [20-24, 27-30]; alternatively, the entire Schiff base metal complex was tethered via axial ligation to H_2N -modified MCM-41 [25-26] or -OOC -modified CMK-3 [31]. Among these studies, there are three examples which report H_2O_2 activation [20,25,31] and three catalytic systems, i.e. $[\text{Mn}^{\text{II}}\text{-Schiff base/MCM-41/t-BuOOH}]$ [28], $[\text{Mn}^{\text{III}}\text{-Schiff base/SBA-15/t-BuOOH}]$ [30] and $[\text{Mn}^{\text{III}}\text{-Schiff base/CMK-3/ H}_2\text{O}_2]$ [31], which use Mn-Schiff base complexes as active catalytic components.

Our group has developed synthetic strategies to prepare active $[\text{Mn}^{\text{II}}\text{-Schiff base}]$ oxidation catalysts covalently grafted onto silica-based [32-34] and carbon-based materials [35-36]. Capitalizing our findings in catalytic oxidations, we point out that for successful H_2O_2 incorporation by grafted Mn-complexes, competitive H_2O_2 dismutation, by either the Mn-center or the inorganic support, should be minimized [32-35]. We have demonstrated also that the catalytic efficiency of such $[\text{Mn}^{\text{II}}\text{-Schiff base}]$ catalysts is switched-on by $\text{CH}_3\text{COONH}_4$ achieving remarkable effectiveness and selectivity towards epoxides [32-35].

Here we present the covalent grafting of $\text{Mn}^{\text{II}}\text{-Schiff base}$ catalysts onto mesoporous nanomaterials MCM-41, SBA-15 and CMK-3 *via* two synthetic approaches. For the silicon-based MCM-41 and SBA-15 inorganic supports, the adopted approach involves two steps: first, Schiff base grafting onto MCM-41 and SBA-15 and second, metalation

of the so-formed [Schiff base@MCM-41] and [Schiff base@SBA-15] hybrid materials. In the case of CMK-3, our present result revealed that to obtain an active and highly rapid [Mn^{II}-Schiff base@CMK-3] catalyst, we had to covalently graft, in one step, the entire [Mn^{II}-Schiff base] catalyst onto CMK-3. For comparison reasons, the ‘two-steps’ synthetic procedure is also discussed herein for CMK-3. We present detailed catalytic data demonstrating that the so-obtained ‘single-site heterogeneous catalysts’ are efficient in alkene epoxidations by H₂O₂ incorporation in the presence of ammonium acetate and selective towards alkene epoxides formation. Considerations/implications concerning the textural features of the obtained catalysts and their catalytic performance are also discussed herein.

2. Experimental

Tetraethylorthosilicate (TEOS) 98%, cetyltrimethylammonium bromide (CTAB) 95%, triblock copolymer Pluronic P123 (EO₂₀PO₇₀EO₂₀, EO = ethylene oxide, PO = propylene oxide) and sucrose were purchased from Sigma-Aldrich. Hydrochloric acid 37%, sulfuric acid 95–97% and sodium hydroxide were purchased from Merck, whereas ethanol (EtOH) 99.5% and aqueous ammonia solution (NH₃) 25 wt% were purchased from Panreac and Fluka, respectively. All substrates were purchased from Aldrich, in their highest commercial purity, stored at 5 °C and purified by passage through a column of basic alumina with methanol as the eluting solvent, prior to use. Hydrogen peroxide was 30% aqueous solution and was purchased from Sigma-Aldrich.

Infrared spectra were recorded on a Spectrum GX Perkin-Elmer FT-IR System. Thermogravimetric analyses were carried out by a Shimadzu DTG-60 analyser using a heat rate of 5 K min⁻¹ and a flow rate of synthetic air carrier gas of 50 cm³ min⁻¹. The N₂ adsorption–desorption isotherms were measured at 77 K on a Sorptomatic 1990, thermo Finnigan porosimeter. Specific surface areas were determined with the Brunauer–Emmett–Teller (BET) method using adsorption data points in the relative pressure (P/P₀) range of 0.05–0.30 and assuming a closely packed BET monolayer. Raman spectra were recorded with a micro-Raman system RM 1000 Renishaw using a laser excitation line at

532 nm (Nd:YAG) in the range 400–2000 cm^{-1} . X-ray powder diffraction data were collected on a D8 Advance Bruker diffractometer using Cu K α (40 kV, 40 mA, $\lambda = 1.54178 \text{ \AA}$) radiation and a secondary beam graphite monochromator. Elemental analyses (C, H, N) were obtained using a Perkin Elmer Series II 2400 elemental analyzer. The manganese amount was determined by flame atomic absorption spectroscopy on a Perkin-Elmer AAS-700 spectrometer. GC analysis was performed using an 8000 Fisons chromatograph with a flame ionization detector and a Shimadzu GC-17A gas chromatograph coupled with a GCMS-QP5000 mass spectrometer. H_2O_2 was added by a digitally controlled syringe pump type SP101IZ WPI over 1 h under stirring. Solution potential E_h was measured by a Metrohm platinum redox electrode (type 6.0401.100). Electron Paramagnetic Resonance (EPR) spectra were recorded with a continuous-wave Bruker ER200D spectrometer at liquid N_2 temperature (77K), equipped with an Agilent 5310A X-Band frequency counter. The spectrometer was running under homemade software based on Lab-View. All measurements were conducted in quartz EPR tubes of 3mm at liquid nitrogen 77K temperature.

2.1 Synthesis and characterization of materials

Schiff base Synthesis. The used Schiff base ligand 1,3-bis[3-aza-3-(1-methyl-3-oxobut-1-enyl)-prop-3-en-1-yl]-2-(4-hydroxy-phenyl)-1,3-imidazolidine, so-called **L** herein, has been synthesized and characterized by our group [37].

MCM-41 Synthesis. The MCM-41 sample was synthesized using CTAB as the surfactant and TEOS as the silica source [38]. In a typical synthesis, 50 g of TEOS added to one liter polyethylene bottle containing 417.5 g of H_2O , 268.5 g of NH_3 (25 wt%) and 10.5 g of CTAB. The resulting mixture was stirred for 30 min and then was heated for 96 h at 353 K under static condition. The product was filtered, rinsed with cold EtOH, dried in air and calcined at 823 K for 5 h with a 2 K/min heating rate to remove the template.

DRIFT-IR (cm^{-1} , selected peaks): 1081: $\nu(\text{Si-O-Si})$; 803 (stress), 463 (bend), 1699 (distorted), 3441 (free): $\nu(\text{Si-OH})$. Thermal analysis shows a weight loss of 0.7 %. This material had an average surface area of ca. $1033 \text{ m}^2 \text{ g}^{-1}$, see Table 1.

SBA-15 Synthesis. The SBA-15 sample was prepared using the triblock copolymer pluronic P123 as the surfactant and tetraethylorthosilicate as the silica source, following synthesis procedure reported by Zhao et al. [9,39]. Specifically, 8.50 g of TEOS added to a solution of 4.0 g P123 copolymer in 150 g of 1.6 M HCl. The mixture was stirred until TEOS was dissolved and then was heated for 22 h at 311 K and subsequently for 24 h at 368 K under static condition. The product was filtered, dried in air (without washing), and calcined at 773 K for 6 h with a 1.5 K/min heating rate to remove the template.

DRIFT-IR (cm^{-1} , selected peaks): 1087: $\nu(\text{Si-O-Si})$; 804 (stress), 468 (bend), 3446 (free), 1637 (destorted): $\nu(\text{Si-OH})$. Thermal analysis exhibits a weight loss of 1.7 %. This material showed an average surface area of ca. $712 \text{ m}^2 \text{ g}^{-1}$, see Table 1.

CMK-3 Synthesis. The synthesis of CMK-3 carbon was performed according to a hard template procedure reported from Jun et al. [40,41]. In particular, 1 g of SBA-15 was added to a solution obtained by dissolving 1.25 g of sucrose and 0.14 g of H_2SO_4 in 5 g of H_2O . The mixture was dried for 6 h at 373 K, and subsequently for 6 h to 433 K. The material was treated again at 373 and 433 K using the same drying procedure after the addition of 0.8 g of sucrose, 0.09 g of H_2SO_4 and 5 g of H_2O . The carbonization was completed by pyrolysis with heating to typically 1173 K under vacuum. After the carbonization, the silica/carbon material was treated twice with 1 M NaOH in 1/1 (v/v) solution of EtOH/ H_2O at 373 K to remove the silica template. The obtained product was filtered, washed with ethanol, and dried at 393 K.

DRIFT-IR (cm^{-1} , selected peaks): 3426: $\nu(\text{C-OH})$; 1707: $\nu(\text{C=O})$; 1572: $\nu(\text{C=C})$; 1356: $\nu(\text{C=O})$; 1163: $\nu(\text{C-H})$ or $\nu(\text{C-O})$; 585: $\nu(\text{O-C=O})$. Thermal analysis exhibits a weight loss of 9.4 %, which is attributed to the decomposition of the surface oxygen groups. The average surface area of this material was ca. $1260 \text{ m}^2 \text{ g}^{-1}$, as listed in Table 1.

Synthesis of modified mesoporous materials. (a) 1 mmol of ligand **L** and 0.85 mmol of (3-chloropropyl)-trimethoxysilane were refluxed for 48 h in 50 ml of MeOH under N_2 at 60 °C leading to **L-OS** silane-precursor. (b) To this, 1.5 g of silica nanoparticles **MCM-41** or **SBA-15** and 5 ml EtOH were added and refluxed at 60 °C for 24 h. After cooling at room temperature, the resulting material **L@MCM-41** or **L@SBA-15** respectively was separated by filtration, washed several times with MeOH and EtOH and dried under

vacuum at 60 °C for 12 h. In the case of **L@CMK-3**, 1.2 mmol of ligand **L**, 1 mmol of (3-chloropropyl)-trimethoxysilane and 0.5 g of **CMK-3** nanoparticles were used applying the same synthetic protocol.

L@MCM-41: Ligand loading: 0.26 mmol g⁻¹ based on elemental and thermogravimetric analysis. DRIFT-IR (cm⁻¹, selected peaks): 1088: $\nu(\text{Si-O-Si})$; 813(stress), 456(bend), 3441(free): $\nu(\text{Si-OH})$; 2965, 2861: $\nu(\text{C-H})$; 1707: $\nu(\text{C=O})$; 1624: $\nu(\text{C=N})$; 1446: $\nu(\text{C=C})$; 1371: $\nu(\text{C-O})$. This material showed an average surface area of ca. 860 m² g⁻¹, see Table 1.

L@SBA-15: Ligand loading: 0.24 mmol g⁻¹ based on elemental and thermogravimetric analysis. DRIFT-IR (cm⁻¹, selected peaks): 1088: $\nu(\text{Si-O-Si})$; 813(stress), 463(bend), 3456(free) $\nu(\text{Si-OH})$; 2965,2853: $\nu(\text{C-H})$; 1707: $\nu(\text{C=O})$; 1624: $\nu(\text{C=N})$; 1453 $\nu(\text{C=C})$; 1371: $\nu(\text{C-O})$. This material showed an average surface area of ca. 442 m² g⁻¹, see Table 1.

L@CMK-3: Ligand loading: 0.34 mmol g⁻¹ based on elemental and thermogravimetric analysis. DRIFT-IR (cm⁻¹, selected peaks): 3404: $\nu(\text{C-OH})$; 2935: $\nu(\text{C-H})$; 1705: $\nu(\text{C=O})$; 1569: $\nu(\text{C=N})$; 1432: $\nu(\text{C=C})$; 1354: $\nu(\text{C-O})$; 1167: $\nu(\text{C-C})$ or $\nu(\text{C-OH})$; 620: $\nu(\text{O-C-O})$. This material showed an average surface area of ca. 792 m² g⁻¹, see Table 1.

Synthesis of single-site heterogeneous catalysts. 0.3 mmol of MnCl₂·4H₂O dissolved in 10 ml MeOH were added to a suspension of 0.5 g **L@MCM-41** in 40 ml MeOH and stirred overnight at room temperature. The resulting heterogeneous catalyst **L@MCM-41-Mn^{II}** was separated by filtration, washed several times with MeOH, EtOH and Et₂O and dried at 60 °C for 3 h. The amount of the bound manganese was determined by back-titration of the remaining amount of metal-ion into the solution and by Atomic Absorption Spectroscopy. Accordingly, the metalation of the hybrid material **L@SBA-15** was achieved resulting in **L@SBA-15-Mn^{II}** catalyst. For **L@CMK-3-Mn^{II}** catalyst, 1.2 mmol of MnCl₂·4H₂O were used for 0.5 g of **L@CMK-3**.

L@MCM-41-Mn^{II}: Metal loading: 0.25 mmol g⁻¹ by flame atomic absorption spectroscopy. DRIFT-IR (cm⁻¹, selected peaks): 1090: $\nu(\text{Si-O-Si})$; 808(stress), 457(bend), 3458(free) $\nu(\text{Si-OH})$; 2966, 2855: $\nu(\text{C-H})$; 1709: $\nu(\text{C=O})$; 1633: $\nu(\text{C=N})$; 1458: $\nu(\text{C=C})$;

1370: $\nu(\text{C-O})$. Thermal analysis exhibits a weight loss of 12.9 %, which corresponds to the combustion of organic ligand **L**. Ligand loading was found to be 0.28 mmol g^{-1} based on elemental and thermogravimetric analysis. This material showed an average surface area of ca. 766 $\text{m}^2 \text{g}^{-1}$, see Table 1.

L@SBA-15-Mn^{II}: Metal loading: 0.22 mmol g^{-1} by flame atomic absorption spectroscopy. DRIFTS-IR (cm^{-1} , selected peaks): 1079: $\nu(\text{Si-O-Si})$; 811(stress), 458(bend), 3450(free): $\nu(\text{Si-OH})$; 2983, 2854: $\nu(\text{C-H})$; 1709: $\nu(\text{C=O})$; 1633: $\nu(\text{C=N})$; 1440: $\nu(\text{C=C})$; 1370: $\nu(\text{C-O})$. Thermal analysis exhibits a weight loss of 10.0 %, which is attributed to the decomposition of ligand **L**. Ligand loading was found to be 0.20 mmol g^{-1} based on elemental and thermogravimetric analysis. This material showed an average surface area of ca. 414 $\text{m}^2 \text{g}^{-1}$ (Table 1).

L@CMK-3-Mn^{II}: Metal loading: 0.26 mmol g^{-1} by flame atomic absorption spectroscopy. DRIFTS-IR (cm^{-1} , selected peaks): 3405: $\nu(\text{C-OH})$; 2983,2927: $\nu(\text{C-H})$; 1703: $\nu(\text{C=O})$; 1565: $\nu(\text{C=N})$; 1432: $\nu(\text{C=C})$; 1353: $\nu(\text{C-O})$; 1170: $\nu(\text{C-C})$ or $\nu(\text{C-OH})$; 532: $\nu(\text{O-C-O})$. Thermal analysis exhibits a weight loss of 13.4 %, corresponding to the decomposition of ligand **L**. Ligand loading was found to be 0.29 mmol g^{-1} based on elemental and thermogravimetric analysis. This material showed an average surface area of ca. 724 g^{-1} , as listed in Table 1.

Organo-silane metalation. In the case of **CMK-3** an alternative method has also been applied with the metalation step being detoured: The **L-OS** silane-precursor was formed according to the procedure described above. (a) 1.2 mmol of ligand **L** and 1.0 mmol of (3-chloropropyl)-trimethoxysilane were refluxed for 48 h in 10 ml of MeOH under N_2 at 60 °C leading to **L-OS** silane-precursor. (b) Then, after cooling at room temperature, 1.2 mmol of $\text{MnCl}_2 \cdot 4\text{H}_2\text{O}$ dissolved in 10 ml MeOH were added to this solution and stirred overnight at room temperature leading to metal precursor **Mn^{II}-L-OS**. (c) To this 0.5 g of **CMK-3** and 5 ml EtOH were added and refluxed at 60°C for 24 h. The resulting material **Mn^{II}-L@CMK-3** was separated by filtration, washed several times with MeOH, EtOH and Et₂O dried under vacuum at 60 °C for 12 h. The catalyst **Mn^{II}-L@CMK-3** was

formed through hydrolysis and co-condensation of the precursor **Mn^{II}-L-OS** with the –OH surface functional groups of **CMK-3**.

Mn^{II}-L@CMK-3: Metal loading: 0.28 mmol g⁻¹ by flame atomic absorption spectroscopy. DRIFTS-IR (cm⁻¹, selected peaks): 3364: ν (O-H); 2922: ν (C-H); 1576: ν (C=N); 1438: ν (C=C); 1366: ν (C-O); 1244: ν (C-C); 1172: ν (C-C); 614: ν (O-C-O). Thermal analysis exhibits a weight loss of 14.5 %, corresponding to the decomposition of ligand L. Ligand loading was found to be 0.32 mmol g⁻¹ based on elemental and thermogravimetric analysis. The average surface area of this material was ca. 35 m²g⁻¹, see Table 1.

2.2 Catalytic Experiments.

Catalytic Protocol. The catalytic solutions were prepared according to the experimental conditions [catalyst : H₂O₂ : alkene : CH₃COONH₄] = [1:2000:1000:1000 μ mol]. The alkene (as substrate, 1 mmol), acetophenone or bromobenzene (as internal standard, 1 mmol), catalyst (1 μ mol of Mn-complex) and CH₃COONH₄ (as additive, 1 mmol) were added in a solvent mixture of acetone/MeOH (450 μ l /400 μ l). H₂O₂ (2 mmol) was added by a digitally controlled syringe pump [SP101IZ WPI] over 30 min to this catalytic solution. The total volume of the catalytic solution was 1 ml. According to the catalysts' loading and their molecular weights, 1 μ mol of **L@MCM-41-Mn^{II}**, **L@SBA-15-Mn^{II}**, **L@CMK-3-Mn^{II}** and **Mn^{II}-L@CMK-3** corresponds to 3.8 mg, 3.7 mg, 3.3 mg and 3.5 mg respectively. The reactions were complete within 24 h, 21 h, 5 h and 1 h for **L@MCM-41-Mn^{II}**, **L@SBA-15-Mn^{II}**, **L@CMK-3-Mn^{II}** and **Mn^{II}-L@CMK-3**, respectively. The progress of the reactions was analyzed by GC-MS, for 20 μ l samples periodically taken from the reaction mixtures. Quantitative GC-analysis provided the substrate conversion and product yield by comparing the integrals of the GC peaks vs. the internal standard integral. When alcohol and ketone were detected as allylic oxidation products, the sample was treated with PPh₃ and measured again by GC-MS according to Shul'pins' procedure [42]. To ensure the identity of the epoxide product, the retention time and spectral data were compared to those of commercially available products. Blank experiments showed that without Mn-catalyst or CH₃COONH₄, oxidation reactions do not occur.

Recycling experiments. The heterogeneous catalysts were tested for their recyclability in new catalytic experiments using cyclooctene as substrate, under the same experimental conditions [catalyst: H₂O₂: substrate: CH₃COONH₄] = [1:2000:1000:1000 μmol] as mentioned above. After the end of each catalytic reaction, 24 h for reactions catalysed by **L@MCM-41-Mn^{II}**, 21 h in the case of the catalyst **L@SBA-15-Mn^{II}** and 5 h and 1 h for reactions catalysed by **L@CMK-3-Mn^{II}** and **Mn^{II}-L@CMK-3**, respectively, the solid catalysts were separated from the reaction mixture by centrifugation, washed three times with MeOH and dried under vacuum (40 °C, 12 h). The mass of each recovered solid catalyst was estimated by mass-weighting. The same mass of each solid was used in each cycle, by running 5 identical catalytic batches followed by centrifugation/washing/drying as described above. Thus for the next use we could weigh exactly 3.8 mg, 3.7 mg, 3.3 mg and 3.5 mg of **L@MCM-41-Mn^{II}**, **L@SBA-15-Mn^{II}**, **L@CMK-3-Mn^{II}** and **Mn^{II}-L@CMK-3** respectively. The recovered solid catalysts were reused for new catalytic systems under the same catalytic conditions.

2.3 EPR study

5 mg powder of each material was used for EPR measurements, that were inserted in 3mm ID quartz tubes (Willmad Glass). For the estimation of the Mn-leaching after catalyst use, the catalytic reaction mixture sample was centrifuged, and 100 μL of the liquid supernatant was used in 3mm ID quartz tubes that were frozen at 77K in liquid N₂. Quantitative estimation of the Mn^{II}-concentration was done by comparison with a MnCl₂ standard in MeOH, using the double integral of the EPR signal.

3. Results and discussion

3.1 Synthesis of the catalysts

The covalent grafting of Mn^{II}-Schiff base catalysts onto mesoporous nanoparticles MCM-41 and SBA-15 was achieved by applying synthetic steps depicted in Scheme 1: i) Schiff base ligand **L** grafting onto MCM-41 and SBA-15 and ii) metalation of the hybrid [**L@MCM-41**] and [**L@SBA-15**] materials. In the first step (see Scheme 1),

derivatization of the Schiff base ligand **L** via its phenolic group with (3-chloropropyl)-trimethoxysilane results to **L-OS** silane-precursor which is grafted -via hydrolysis and co-condensation- onto **MCM-41** and **SBA-15** providing the hybrid materials **L@MCM-41** and **L@SBA-15** respectively. Subsequently, during the second synthetic step, Mn^{II} -complexation to grafted ligands furnished the **L@MCM-41-Mn^{II}** and **L@SBA-15-Mn^{II}** catalysts. The same procedure was applied to **CMK-3** giving the corresponding **L@CMK-3-Mn^{II}** catalyst.

However, very recently we have found that metalation of grafted ligands onto carbon-based supports results in totally inactive materials in catalytic epoxidations [35]. This was attributed to Mn^{II} -spoliation by the free $-\text{COOH}$ groups of the activated carbon support blocking the desirable Mn^{II} -complexation with the grafted ligands in order to form the active catalytic centre [35]. Here to exclude such possibility when dealing with **CMK-3**, an alternative synthetic strategy was adopted which allowed the covalent grafting of the entire [Mn^{II} -Schiff base] catalyst onto **CMK-3** in one step (see Scheme 2). More specifically derivatization of the Schiff base ligand **L** forms the **L-OS** silane-precursor; then its metalation with Mn^{II} -ions results to **Mn^{II}-L-OS**. The so-formed metal complex **Mn^{II}-L-OS** is grafted to the solid support **CMK-3** by its propyl-trimethoxysilane moieties which allow covalent attachment via hydrolysis and co-condensation with the -OH surface functionalities of **CMK-3** (Scheme 2). This catalyst, prepared by grafting of the preformed Mn^{II} -complex to **CMK-3**, is herein codenamed as **Mn^{II}-L@CMK-3** (Scheme 2). Characterisation and catalytic behaviour of both **L@CMK-3-Mn^{II}** and **Mn^{II}-L@CMK-3** materials is detailed and discussed hereafter.

3.2 Structural and textural characterisation

FT-IR study: The DRIFT-IR spectra of the developed catalysts show characteristic bands, which are attributed to various structural components of the present materials, i.e. to the support scaffold as well as to the grafted Schiff base ligand **L**. That is, when the DRIFT-IR spectra of **L@MCM-41**, **L@SBA-15** and **L@CMK-3** were compared to those of the

parent materials **MCM-41**, **SBA-15** and **CMK-3** respectively, new bands can be observed which are attributed to the anchored ligand **L**. More specifically, in the spectra of grafted ligand **L@MCM-41**, **L@SBA-15** and **L@CMK-3**, the bands observed at 1707, 1707 and 1705 cm^{-1} respectively are attributed to $\nu(\text{C}=\text{O})$ stretching vibrations of the Schiff base ligand **L**. The band, which is observed in both **L@MCM-41** and **L@SBA-15** hybrids at 1624 cm^{-1} , is assigned to the $\nu(\text{C}=\text{N})$ stretching of the Schiff base **L** as well; this band, in the case of **L@CMK-3** material, is shifted at 1569 cm^{-1} and highly contributed by conjugated $\nu(\text{C}=\text{C})$ vibrations from the carbonaceous **CMK-3** support. In the spectra of both catalysts **L@MCM-41-Mn^{II}** and **L@SBA-15-Mn^{II}**, the abovementioned vibrations $\nu(\text{C}=\text{O})$ and $\nu(\text{C}=\text{N})$ are observed at 1709 and 1633 cm^{-1} , being clearly shifted when compared with the non-metalated materials **L@MCM-41** and **L@SBA-15**; this behaviour indicates coordination of the Mn^{II} with the imine-nitrogen and keto-oxygen of the attached ligand **L** [33,35,43]. In the spectra of **Mn^{II}-L@CMK-3**, the $\nu(\text{C}=\text{O})$ band was slightly shifted when compared with the corresponded band of the non-metalated **L@CMK-3** material; however, the $\nu(\text{C}=\text{N})$ stretching, which is more sensitive in metalation, is observed at 1576 cm^{-1} taking in to account that, in **L@CMK-3**, is observed at 1569 cm^{-1} . Based on these, we conclude that, in **Mn^{II}-L@CMK-3** catalyst, the Mn^{II} is selectively bound to the grafted Schiff base ligand **L** ensuring the presence of the entire active catalytic centre onto the **CMK-3** surface [35]. As concerned the vibrations $\nu(\text{C}=\text{O})$ and $\nu(\text{C}=\text{N})$ of **L@CMK-3-Mn^{II}**, they are shifted as well, when compared with the corresponding bands of the non-metalated ligand **L@CMK-3**, indicating also coordination of the Mn^{II} with attached ligand **L** [33,35,43].

Thermal analysis: The thermograms of the silica-based catalysts **L@MCM-41-Mn^{II}** and **L@SBA-15-Mn^{II}** show a 13.6 % and 13.5 % weight loss respectively, in the range of 130-400 °C, which are attributed to the decomposition of the anchored organic molecules (Figure 2 A, B). The pristine **CMK-3** material is dominantly composed by carbon and oxygen, with a percentage content of 87.9% and 9.4%, respectively. The surface oxygen groups are generated from the incomplete dehydration of the sucrose carbon source [31]. The thermograms of the **L@CMK-3-Mn^{II}** and **Mn^{II}-L@CMK-3** (Figure 2 C, D)

materials show a 22.3 % and 23.9 % weight loss respectively, in the range of 130-400 °C. Given that CMK-3 support bears 9.4-10.0 % surface oxygen functionalities which are decomposed in the same temperature region (130-400 °C), the rest weight loss of 13.4 and 14.5 % for **L@CMK-3-Mn^{II}** and **Mn^{II}-L@CMK-3** respectively can be reasonably ascribed to the decomposition of the anchored organic ligand **L** (See Table 1).

Nitrogen Sorption Isotherms: N₂ adsorption-desorption isotherms for all materials are shown in Figures 3a, 4a and 5a; the Brunauer-Emmett-Teller (BET) surface area values as well as the pore characteristics of pristine and modified materials are listed in Table 1.

In case of the silicon-based catalysts (Figure 3a and 4a), all isotherms are type IV which is characteristic of mesoporous materials; moreover, the adsorption curve exhibit a well-defined capillary condensation step indicating filling of uniform mesopores. The beginning of this step for the **L@MCM-41**, **L@MCM-41-Mn^{II}** and **L@SBA-15**, **L@SBA-15-Mn^{II}** materials occurs at a lower pressure range compare to the pristine materials **MCM-41** and **SBA-15** respectively. This behavior suggests a decrease in pore size [44,45] due to the Schiff base ligand **L** grafting and subsequent Mn^{II}-coordination. Indeed, from the BJH pore size distribution (Figure 3b and 4b), a significant decrease in pore diameter and total pore volume is observed in modified materials compare to the pristine materials (Table 1). In case of the pristine **CMK-3** and the carbon-based materials **L@CMK-3** and **L@CMK-3-Mn^{II}**, which were prepared by the same synthetic procedure as the **L@MCM-41**, **L@MCM-41-Mn^{II}** and **L@SBA-15**, **L@SBA-15-Mn^{II}** materials (see Scheme 1), the isotherms are also type IV. However, the isotherm of **Mn^{II}-L@CMK-3**, this was prepared after grafting of the entire Mn^{II}-Schiff base catalyst onto **CMK-3** in one step, indicates a nonporous material. The specific surface area for this **Mn^{II}-L@CMK-3** catalyst shows a dramatic collapse, e.g., from 1260 m²g⁻¹ in pristine **CMK-3** to 35 m²g⁻¹ in **Mn^{II}-L@CMK-3**. We notice that analogous behaviour was showed when the entire Mn^{II}-Schiff base catalyst was grafted by similar method onto the surface of activated carbon **ACox** [35] where the specific surface area of **ACox** of 687 m²g⁻¹ became 21 m²g⁻¹ in **Mn^{II}-L@ACox** indicating formation of compacted carbon layers with practically zero porosity [35].

The specific surface area (SSA in Table 1) of 1033, 712 and 1260 m²g⁻¹ for the pristine **MCM-41**, **SBA-15** and **CMK-3** materials respectively, was decreased significantly after Schiff base ligand **L** grafting onto their surface, exhibiting surface area 860, 442 and 792 m²g⁻¹ for **L@MCM-41**, **L@SBA-15** and **L@CMK-3** respectively. A further decrease was observed after Mn^{II}-coordination, calculated to 766, 414 and 724 m²g⁻¹ for **L@MCM-41-Mn^{II}**, **L@SBA-15-Mn^{II}** and **L@CMK-3-Mn^{II}** respectively, see Table 1. This 26-43% decrease of the specific surface area provides evidence that the pores are filled by the Mn^{II}-complex without blocking the pores [8].

Raman study: Raman spectra of **CMK-3**, **L@CMK-3**, **L@CMK-3-Mn^{II}** and **Mn^{II}-L@CMK-3** materials are shown in Figure 6. The spectra of all samples exhibit the two characteristic peaks of carbon-based materials at 1598 cm⁻¹ and 1340 cm⁻¹ corresponding to the well-known G- and D-band vibrations, respectively. More specifically, the first band at 1598 cm⁻¹ (G-band) derives from the in-plane-bond stretching motion of pairs of sp² carbon atoms, while the second band at 1340 cm⁻¹ (D-band) which only becomes active in the presence of disorder, derives from sp² edge plane breathing vibrations [46]. The relative intensity ratio of D and G band (I_D/I_G) has been constantly used as a measure of structural graphitization order and it is a tool to identify structural changes in carbon materials due to their treatment. This ratio has similar value ~0.9 for all samples and it is typical for CMK-3 structures [47] indicating a mainly disordered carbon structure. Overall these Raman data suggest that the graphitized features of carbon remains unimpaired after the grafting procedure.

Powder X-ray diffraction (XRD): The XRD patterns of all samples are shown in Figure 7. In case of pristine materials **MCM-41**, **SBA-15** and **CMK-3** the patterns exhibit three characteristic peaks which can be indexed to the (100), (110) and (200) reflections of the hexagonal space group (P6mm). This indicates a hexagonal arrangement of the mesopores of **MCM-41** and **SBA-15** and a hexagonal arrangement of interconnected carbon nanorods in case of **CMK-3**, which is the negative replica of **SBA-15**. These peaks are still observed in **L@MCM-41**, **L@SBA-15**, **L@CMK-3**, **L@MCM-41-Mn^{II}**, **L@SBA-15-Mn^{II}** and **L@CMK-3-Mn^{II}** indicating that the ordered structure of pristine

materials was retained after the grafting of the Mn^{II}-Schiff base catalyst on their surface. On the other hand, these reflections are not visible in the pattern of **Mn^{II}-L@CMK-3**. However, such behavior does not necessarily suggest the damage of the structural order of CMK-3 support; it could be correlated to some density effects originating from the material constituting the carbon walls and the material filling/coating the pore regions. Similar effect has already been discussed in previous studies dealing with metal oxide incorporation into the pores of silicate and carbon mesostructures [41, 48-51]. According to these studies the loss in intensity was due to the introduction of scattering material into the pores which leads to an increased phase cancellation between scattering from walls and the pore regions [41, 48-51]. That is, the absence of XRD reflections can be attributed to a very high filling of the pores. In our case here, **L@CMK-3-Mn^{II}** presents reflections indicating a hexagonal arrangement as expected, while **Mn^{II}-L@CMK-3** losses these peaks. Given that the experimental conditions for the synthesis of **Mn^{II}-L@CMK-3** is analogous for that of **L@CMK-3-Mn^{II}**, putative damage of structural order seems to be unfounded. Thus, the loss of the reflections probably originated from the pore filling of **CMK-3** with the active Mn^{II}-L catalyst. The direct question, why the ligand L doesn't fill the **CMK-3** pores –see for example the **L@CMK-3** material-, while the entire Mn^{II}-L catalyst does, it could be addressed taking into account a possible better mobility of the Mn^{II}-L complex within the pores *vs.* the organic ligand L alone.

3.3 Catalytic Study

The developed Mn^{II}-containing materials **L@MCM-41-Mn^{II}**, **L@SBA-15-Mn^{II}**, **L@CMK-3-Mn^{II}** and **Mn^{II}-L@CMK-3** were evaluated as catalysts for alkene epoxidation with H₂O₂. Typical reaction conditions employed in these experiments were 1 equiv. of catalyst, 2000 equiv. of H₂O₂ 30% delivered by the syringe pump during 30 min into an [acetone:methanol] (0.45ml:0.40ml) solution, 1000 equiv. of substrate and ammonium acetate (1000 equiv.) at room temperature. The heterogeneous catalysts described here required ammonium acetate as additive to generate high catalytic activity in analogous way to previous catalysts based on non-heme-Mn^{II}-complexes [32-35,52].

Catalytic Oxidation Yield and TONs: The heterogeneous Mn^{II}-based catalysts presented significant catalytic activity and high selectivity towards formation of epoxides (the mass balance is 98-100%) in most of the cases (see Table 2). Thus, cyclooctene oxidation provides a 100% selectivity for cis-cyclooctene epoxide with 56.0%, 24.5%, 24.0% and 50.6% yield (100% m.b.) catalysed by **L@MCM-41-Mn^{II}**, **L@SBA-15-Mn^{II}**, **L@CMK-3-Mn^{II}** and **Mn^{II}-L@CMK-3** respectively (see Figure 10 A). Cyclohexene epoxide formation, from cyclohexene oxidation, was found to be 50.2%, 46.0%, 33.0% and 37.8% catalysed respectively by **L@MCM-41-Mn^{II}**, **L@SBA-15-Mn^{II}**, **L@CMK-3-Mn^{II}** and **Mn^{II}-L@CMK-3**; however, in epoxidation catalysed by **Mn^{II}-L@CMK-3**, a small amount of 2-cyclohexene-1-ol (3.0%) was detected derived probably by allylic oxidation of cyclohexene. This amount of 2-cyclohexene-1-ol was identical to that for PPh₃-treated sample following the Shul'pins' procedure [42]; this treatment ensures that if any hydroperoxides have been formed as primary-product, this has been completely transformed into the alcohol- and ketone-oxidation products [42,53]. Two epoxides (cis- and trans-) were the main products derived from epoxidation of the electron-rich double bond in 1,2-position of limonene. The total yield of 1,2-epoxides was 70.0%, 51.7%, 41.6% and 63.4% catalysed by **L@MCM-41-Mn^{II}**, **L@SBA-15-Mn^{II}**, **L@CMK-3-Mn^{II}** and **Mn^{II}-L@CMK-3** respectively. Considerable amounts of products formed by allylic oxidation of the limonene ring have also been observed and have been identified as the corresponding derivative of cyclohexene-1-ol (7.9-13.7%). No formation of epoxides derived from the more accessible but less electron-rich double bond in 8,9-position has been observed. However, the epoxidation was clearly the major reaction path resulting mainly in 1,2-epoxides (see Table 2, Figure 8 A). Thus, the total yield of catalytic limonene oxidation (1,2-epoxide plus cyclohexene-1-ol derivative) was varied from 49.7% to 77.9%. Hexene-1, which contains a less electron-rich double bond, is a rather hard oxidation substrate, showing low epoxide yields 6.9%, 6.0%, 4.9% and 6.5% for **L@MCM-41-Mn^{II}**, **L@SBA-15-Mn^{II}**, **L@CMK-3-Mn^{II}** and **Mn^{II}-L@CMK-3** respectively. Oxidation of cis-stilbene catalysed by **L@MCM-41-Mn^{II}**, **L@SBA-15-Mn^{II}**, **L@CMK-3-Mn^{II}** and **Mn^{II}-L@CMK-3** provides only cis-epoxide with 46.0%, 18.4%, 45.8% and 18.5% yield respectively. All catalysts studied herein showed 100% selectivity towards the formation of epoxides in catalytic oxidations of styrene, trans-β-

methylstyrene, α -pinene, cyclopentene and 1-methyl-1-cyclohexene with yields 3.0-11.2%, 10.0-31.5%, 27.9-41.8%, 19.5-37.3% and 13.3-36.6% respectively (Table 2, Figure 8 A, B). In these cases a superior catalytic performance has been achieved by **L@MCM-41-Mn^{II}** and **Mn^{II}-L@CMK-3** heterogeneous catalysts. Detailed catalytic data are provided in Table 2.

Comparing the TONs achieved by **L@MCM-41-Mn^{II}**, **L@SBA-15-Mn^{II}**, **L@CMK-3-Mn^{II}** and **Mn^{II}-L@CMK-3**, we observe that **L@MCM-41-Mn^{II}** provides the highest TON values for all evaluated substrates with exception trans- β -methylstyrene and cyclopentene epoxidation (Figure 9 A, B). This remarkable catalytic performance is outcompeted by the carbon-based catalyst **Mn^{II}-L@CMK-3**. When we compare the TONs achieved by silicon-based Mn^{II}-catalysts **L@MCM-41-Mn^{II}** and **L@SBA-15-Mn^{II}**, we notice in general, a superior catalytic performance of **L@MCM-41-Mn^{II}** (Figure 9 A, B). When, in analogous way, we compare the TONs yielded by catalysts attached on **CMK-3** matrix, **L@CMK-3-Mn^{II}** and **Mn^{II}-L@CMK-3**, we observe higher TONs values in epoxidations catalysed by **Mn^{II}-L@CMK-3** with except the cis-stilbene epoxidation. **Mn^{II}-L@CMK-3** was prepared by grafting of the preformed entire Mn^{II}-Schiff base complex to **CMK-3**, while **L@CMK-3-Mn^{II}** was developed by a two-step synthetic procedure constituted by ligand grafting (i) and followed by metalation (ii). It is highlighted that when this two-step synthetic strategy was adopted for prepared analogous Mn^{II}-catalysts supported on activated carbon surface **ACox**, the obtained catalysts were totally inactive in alkene epoxidations with H₂O₂. This was attributed to Mn^{II}-spoliation by the free -COOH groups of the activated carbon support blocking the formation of the active Mn^{II}-L [35]. However, here the corresponding **L@CMK-3-Mn^{II}** hybrid developed on carbonaceous **CMK-3** matrix presents considerable catalytic performance which is equivalent to/or outcompetes **L@SBA-15-Mn^{II}** catalyst (Figure 9 A, B). The observed catalytic activity of **L@CMK-3-Mn^{II}** further strengths our spectral data that the active Mn^{II}-L catalyst has been formed. This happened because the surface oxygen functionalities offered by the non-oxidized **CMK-3**, are not able to trap Mn^{II}, i.e. inhibiting in this way, the formation of active catalyst. Thus, probably the lack of

carboxylates on the surface of **CMK-3** permitted to develop the active carbon-based catalyst **L@CMK-3-Mn^{II}** by the two-step synthetic procedure.

Catalytic Kinetics and TOFs: Figure 10 presents the time-course profiles of the catalysts **L@MCM-41-Mn^{II}**, **L@SBA-15-Mn^{II}**, **L@CMK-3-Mn^{II}** and **Mn^{II}-L@CMK-3** during oxidation reaction of cyclohexene, in conjunction with the redox potential of solution E_h (versus standard hydrogen electrode SHE). In the case of **L@MCM-41-Mn^{II}**, E_h was +388 mV at the beginning of the reaction; after 1 h, it dropped at +265 mV with a 31.6% total oxidation yield and eventually, after 24 h reaction time, it approached a E_h =+223 mV and a 50.2% yield. The **L@SBA-15-Mn^{II}**-catalysed reaction gave at $t=0$, +388 mV, dropping at +263 mV after 1 h with a yield 26.7% and finally, after 21 h reaction time, the values were E_h =+225 mV with a 46.0% yield. In the case of **L@CMK-3-Mn^{II}**, at $t=0$, E_h was +388 mV, decreasing to +248 mV after 1 h with a total yield 27.2% and finally after 5 h, E_h approached +221 mV with a 33.0% cyclohexene epoxide formation. And at the beginning of the reaction catalysed by **Mn^{II}-L@CMK-3**, E_h was +385 mV and after 1 h reaction time, it decreased at E_h =+225 mV with a total 37.8% epoxide yield. The time-course profiles of the catalysts are analogous for all the substrates that have been used. That is, the oxidation reactions catalysed by **L@CMK-3-Mn^{II}** and **Mn^{II}-L@CMK-3** were practically accomplished within 5 h and 1 h respectively and the reactions catalysed by **L@MCM-41-Mn^{II}** and **L@SBA-15-Mn^{II}** were accomplished within 24 h and 21 h respectively.

Taking into account these kinetic data and TONs achieved by each catalyst, we observe that the carbon-based heterogeneous catalyst **Mn^{II}-L@CMK-3** shows remarkably higher TOFs (ranged from 65-634 h⁻¹) vs. the carbon-based catalyst **L@CMK-3-Mn^{II}** (TOFs 9.8-99.6 h⁻¹) and even higher when compared to those achieved by the silicon-based **L@MCM-41-Mn^{II}** (TOFs 2.9-32.5 h⁻¹) and **L@SBA-15-Mn^{II}** (TOFs 1.4-29.6 h⁻¹) catalysts (Figure 11). These findings are in accordance with our previous studies, where carbon-based heterogeneous catalysts showed remarkably higher TOFs vs. the corresponding silica-based catalysts [35]. Moreover, the present carbon-based catalyst onto **CMK-3**, **Mn^{II}-L@CMK-3**, shows even higher TOFs than the corresponding

catalyst onto activated carbon **ACox**, **Mn^{II}-L@ACox** [35]. In general, **Mn^{II}-L@CMK-3** catalyst provides slightly lower TONs than the **Mn^{II}-L@ACox**, however, it is more rapid than **Mn^{II}-L@ACox** resulting finally in higher TOFs. It is possible that this feature is correlated with the practically zero porosity of these catalysts, i.e. specific surface area of 21 m²g⁻¹ for **Mn^{II}-L@ACox** and 35 m²g⁻¹ for **Mn^{II}-L@ACox**. This suggestion is further supported by the fact that **L@CMK-3-Mn^{II}** catalyst with SSA=724 m²g⁻¹ exhibited activity comparable to **Mn^{II}-L@ACox** provides 5 to 10-times lower TOFs than **Mn^{II}-L@ACox**.

Recyclability of the Catalysts: Reuse of heterogeneous catalysts remains always a challenge in catalytic technology. Here, the heterogeneous catalysts **L@MCM-41-Mn^{II}**, **L@SBA-15-Mn^{II}**, **L@CMK-3-Mn^{II}** and **Mn^{II}-L@CMK-3** were tested for their recyclability by repeated re-covering and re-using of the solid catalysts in new catalytic systems for cyclooctene epoxidation. A [catalyst:H₂O₂:substrate:additive]=[1:2000:1000:1000] molar ratio was used in an acetone/MeOH (450 μl /400 μl) solvent mixture. After each catalytic run, which was completed in 24 h for **L@MCM-41-Mn^{II}**, 21 h for **L@SBA-15-Mn^{II}** and 5 h and 1 h for **L@CMK-3-Mn^{II}** and **Mn^{II}-L@CMK-3** respectively, each catalyst was recovered by centrifugation, washed, dried and reused under the same catalytic conditions given in Table 3.

According to Table-3, the carbon-based catalysts **Mn^{II}-L@CMK-3** and **L@CMK-3-Mn^{II}** presented some recyclability, in contrast to the silicon-based catalysts **L@MCM-41-Mn^{II}** and **L@SBA-15-Mn^{II}** which showed a total loss of their catalytic activity (>99%). More specifically, **Mn^{II}-L@CMK-3** presented <50% loss of the catalytic activity during the 2nd run achieving overall 721 TONs for cyclooctene oxidation and **L@CMK-3-Mn^{II}** showed some activity during the 2nd catalytic run.

Monitoring of the state of the solid bearing the Mn-catalyst and Mn-leaching in has been done with two independent protocols as follows:

[i] monitoring leaching of catalytically active species in solution: a) filtering out the solid catalyst after 1 or 1/2h of reaction and then b) monitoring the eventual catalytic performance of the filtrate's solution by GC [33]. The data showed that no evolution of the studied reactions was observed in the filtrate. This proved that no leaching of $[\text{Mn}^{\text{II}}\text{-L}]$ occurs.

[ii] In accordance with the results in method [i], EPR spectroscopy, revealed that Mn^{II} -atoms (not Mn-L) did leach in the solution. More specifically, EPR was used to study the Mn -centers in our Mn -catalysts, unused and recycled, as well as the filtrate's solution of the catalytic reactions.

In Figure 12A (solid lines) we present 77K EPR spectra of the 'as prepared' unused catalysts **L@CMK-3- Mn^{II}** , **$\text{Mn}^{\text{II}}\text{-L@CMK-3}$** , **L@SBA-15- Mn^{II}** and **L@MCM-41- Mn^{II}** . The carbon-based materials are characterized by a broad Gaussian derivative centered at $g \sim 2$, while the Si-based materials, SBA and MCM-41 show 6-line EPR spectra with resolved $\text{Mn}^{\text{II}}(S=5/2, I=5/2)$ hyperfine splittings. Thus EPR shows that the **L@CMK-3- Mn^{II}** sample bears highly clustered Mn -complexes resulting in the strong broadening that masks the $\text{Mn}^{\text{II}}(S=5/2, I=5/2)$ hyperfine splittings. In contrast **$\text{Mn}^{\text{II}}\text{-L@CMK-3}$** shows a Mn -spectrum with a moderate surface clustering. The **L@SBA-15- Mn^{II}** and **L@MCM-41- Mn^{II}** show resolved $\text{Mn}^{\text{II}}(S=5/2, I=5/2)$ spectra. The resolved semiforbidden ^{55}Mn -hyperfine features i.e. the weak sharp lines between the main sextet lines, are typical for the monomeric $\text{Mn}^{\text{II}}\text{-L}$ complex, showing that these signals originate mainly from the active catalytic component [Mn^{II} -Schiff base] grafted on a solid matrix [36].

The EPR data in Figure 12A show that the Mn -concentration on **L@SBA-15- Mn^{II}** and **L@MCM-41- Mn^{II}** is lower than in CMK-3 based materials. **L@SBA-15- Mn^{II}** has the lower Mn -content. These trends are in accordance with the loadings reported in the Table 1.

In Figure 12B we present the % of Mn^{II} leached in the filtrate's solution after a first use of our catalysts, i.e. calculated as the ratio of Mn^{II} released in solution vs. the initial Mn^{II} in each catalytic material. From the lineshape of the EPR spectra we conclude that the

leached Mn^{II} -species corresponds to free Mn^{II} solvated ion. The Mn^{II} remaining on the recycled materials is detected by EPR in Figure 12A(dotted-lines). Accordingly, the data in Figure 12B reveal that **L@CMK-3-Mn^{II}** shows the highest percentage of Mn^{II} -ions released in the catalytic solution, while **L-Mn^{II}-L@CMK-3** shows the lowest Mn^{II} -ions leaching. This indicates that in **L@CMK-3-Mn^{II}** a significant amount of Mn^{II} -ions were loosely associated with the CMK-3 surface groups, other than L. That is, .addition of Mn ions in the **L@CMK-3** material, results in casual Mn-coordination on CMK-3 surface sites, not only on L-ligands. In contrast **Mn^{II}-L @ CMK-3** seems to be more resilient to leaching i.e. since all the Mn-centers are anchored on the CMK-3 surface *via* the preformed [Mn^{II}-Schiff base] complex. This specific Mn-coordination in **Mn^{II}-L@CMK-3** and its lower-loss of Mn-ions is in accordance with the better activity and recyclability respectively of the L-Mn^(II)@ CMK-3 vs, the L@ CMK-3-Mn^(II).

As concerned the **L@SBA-15-Mn^{II}** and **L@MCM-41-Mn^{II}**, considerable amounts of Mn^{II} -ions have been detected in their filtrate's solution after a first use (Figure 12B). For example, the **L@MCM-41-Mn^{II}** despite its good catalytic performance during the first catalytic use shows 55% of Mn-loss after this use, while **L@SBA-15-Mn^{II}** has 22% Mn-loss of Mn^{II} . At this point we notice, however, this Mn-ions leaching from **L@SBA-15-Mn^{II}** and **L@MCM-41-Mn^{II}** does not fully explain their complete inhibition inactivity during the second catalytic run i.e. since a non negligible fraction of Mn remained on the solid matrix. In this context we undertook a close inspection of the ⁵⁵Mn-EPR spectrum, and this revealed the in **L@MCM-41-Mn^{II}** the Mn^{II} centers remaining on the solid, have an EPR hyperfine pattern where the semiborbidden, weak-sharp signals superimposed on the main hyperfine line are lost see inset in Figure 12A. This indicates that these Mn^{II} -centres although still associated to the MCM-41 matrix after catalytic use, they are *not* any more coordinated to L, but have a no-specific coordination environment. This crucial observation points to an oxidative destruction of the active [Mn^{II}-Schiff base] catalytic center of **L@MCM-41-Mn^{II}** and **L@SBA-15-Mn^{II}** i.e. caused by their longer residence under strongly oxidative conditions i.e. 24 and 21 h respectively. In contract in the recycled **L-Mn^{II}@CMK-3**, the remaining Mn^{II} -centers seem to retain their coordination

to L, as in the unused catalyst, further substantiating the observed catalytic activity in a second run.

Performance considerations/-implications:

From the synthetic point of view, the covalent grafting of Mn^{II}-Schiff base catalysts onto mesoporous silicon-based supports MCM-41 and SBA-15 was achieved by applying two discrete synthetic steps: i) Schiff base ligand L grafting onto MCM-41 and SBA-15 and ii) metalation of the hybrid materials obtaining the **L@MCM-41-Mn^{II}** and **L@SBA-15-Mn^{II}** catalysts. This two-step procedure, when applied on carbon-based supports, resulted in totally inactive materials in catalytic epoxidations. This was because of Mn^{II} coordination to the free carboxylate groups of the activated by oxidation carbon supports. To affront this, we have developed an alternative synthetic strategy which allowed the covalent grafting of the entire [Mn^{II}-Schiff base] catalyst onto the carbonaceous matrix in one step. Here, both one- and two-step procedures have been applied to CMK-3 resulting in **Mn^{II}-L@CMK-3** and **L@CMK-3-Mn^{II}** materials respectively; based on our findings here, both are active in alkene catalytic epoxidations with H₂O₂. This is attributed to the nature of the **CMK-3** carbonaceous support; the non-oxidized CMK-3 offers oxygen functionalities for surface grafting, at the same time being devoid of carboxylates that would trap Mn^{II}, thus allowing the formation of the active catalyst.

Here we can make a distinction for the materials **L@MCM-41-Mn^{II}**, **L@SBA-15-Mn^{II}** and **L@CMK-3-Mn^{II}** prepared by *the two-step* procedure. Based on the present BET, XRD data, we conclude that, after the grafting of the Mn^{II}-Schiff base catalyst on their surface, a) the ordered structure of pristine materials was retained and b) they are still porous. A 26-43% decrease of SSA indicates that the pores are filled by the Mn^{II}-complex without blocking the pores.

According to the *one step procedure*, the **Mn^{II}-L@CMK-3** catalyst has been prepared. **Mn^{II}-L@CMK-3** is a nonporous material which lost the XRD reflections of the pristine CMK-3. This behavior, as discussed herein, does not necessarily suggest the damage of the structural order of CMK-3 and it has been probably originated from the pore filling of CMK-3 with the active Mn^{II}-L catalyst.

Comparing the experimental conditions between the *one-step* and *two steps* synthetic processes, both require *similar thermal treatment* and *starting materials*. It is obvious that a putative damage of structural order in **Mn^{II}-L@CMK-3** is unfounded. However, the raised question why the one step procedure leads to nonporous material is still open. In one step synthesis, the grafting moiety is the entire Mn^{II}-L complex, while in the two step one, the initially grafting component is the organic ligand L. If, in **Mn^{II}-L@CMK-3**, Mn^{II}-L fills the pores of CMK-3, why, in **L@CMK-3**, L does not fill the pores completely, as indicated by SSA, blocking them? With data at hand, an acceptable answer is a possible better mobility and/or affinity of the Mn^{II}-L complex within the pores of CMK-3 *vs.* the organic ligand L. This could result, in the case of **Mn^{II}-L@CMK-3**, in completely filling of the pores and the formation of a compact structure. More studies are needed to prove and control this phenomenon.

The present single-site heterogeneous Mn-catalysts have been evaluated for alkene epoxidation with H₂O₂ in presence of the required CH₃COONH₄. In these systems also, CH₃COONH₄ plays a key role on the non-heme-Mn^{II}-catalysts worked with H₂O₂, generating the catalytic efficiency of Mn^{II}-catalysts as reported in our previous studies [32-35, 37, 52, 54]. In details, firstly CH₃COO⁻ abstracts proton from H₂O₂ promoting its coordination to Mn^{II} and formation of Mn^{II}-OOH species; subsequently, NH₄⁺, by acting as a proton-donor to Mn^{II}-OOH, accelerates heterolytic O-O cleavage forming the active Mn^{IV}=O species which finally catalyses alkene epoxidation [35].

To have an overview of the performance of the developed here **L@MCM-41-Mn^{II}**, **L@SBA-15-Mn^{II}**, **L@CMK-3-Mn^{II}** and **Mn^{II}-L@CMK-3** catalysts, it is noted that **L@MCM-41-Mn^{II}** provides the highest TONs values for almost all the evaluated substrates (Figure 9 A, B). This remarkable catalytic performance is outcompeted by the carbon-based catalyst **Mn^{II}-L@CMK-3** which presents by far one of the best catalytic performances of Mn-Schiff base complexes covalently grafted onto CMK-3 matrix with H₂O₂ [31]. When, we direct compare the TONs yielded by **L@CMK-3-Mn^{II}** and **Mn^{II}-L@CMK-3**, we observe higher TONs values in epoxidations catalysed by **Mn^{II}-L@CMK-3**. **Mn^{II}-L@CMK-3** shows also remarkably higher TOFs (ranged from 65-634 h⁻¹) *vs.* the **L@CMK-3-Mn^{II}** catalyst (TOFs 9.8-99.6 h⁻¹) and even higher when

compared to those achieved by **L@MCM-41-Mn^{II}** (TOFs 2.9-32.5 h⁻¹) and **L@SBA-15-Mn^{II}** (TOFs 1.4-29.6 h⁻¹) catalysts. Practically, the reactions catalysed by **L@CMK-3-Mn^{II}** and **Mn^{II}-L@CMK-3** were accomplished within 5 h and 1 h respectively and the reactions catalysed by **L@MCM-41-Mn^{II}** and **L@SBA-15-Mn^{II}** were accomplished within 24 h and 21 h respectively. Generally, this trend is in accordance with our previous studies where carbon-based heterogeneous catalysts showed remarkably higher TOFs vs. the corresponding silica-based catalysts [35], attributable to the nature of the supports. However, comparing the two CMK-3-based catalysts **Mn^{II}-L@CMK-3** and **L@CMK-3-Mn^{II}**, the observed high rapidity of **Mn^{II}-L@CMK-3** is probably correlated with its practically zero porosity. Such effect could be attributable to possible diffusion limits of reagents and/or products into the porous materials served as catalysts in the epoxidation reactions studied.

Overall the percent data provide critical clues on the factors that determine the overall catalytic performance of the hybrids: [i] amount of Mn-coordinated on L vs. Mn-coordinated on non-specific surface sites, [ii] resilience of the Mn-coordinated on L to catalytic harassment plays a key role, [iii] porosity profile is key-factor in heterogeneous catalytic reactions controlling the reaction time.

4. Conclusions

In this study, we present the development of new heterogeneous catalysts via covalent attachment of Mn(II)-Schiff base complexes onto mesoporous MCM-41, SBA-15 and CMK-3 supports. This has been done via two different synthetic protocols: a) a *two steps procedure* which includes grafting of the Schiff base ligand **L** onto the supports and subsequent metalation of the hybrid materials and b) an *one step procedure* which allows the covalent grafting of the entire Mn^{II}-Schiff base catalyst onto the carbonaceous support. The *two steps procedure* resulted in the porous **L@MCM-41-Mn^{II}**, **L@SBA-15-Mn^{II}** and **L@CMK-3-Mn^{II}** single-site Mn-catalysts and the *one step procedure* provided the non-porous catalyst **Mn^{II}-L@CMK-3**. All the catalysts were evaluated for alkene epoxidation with H₂O₂ as oxidant and CH₃COONH₄ as additive. They are effective indicating that the active Mn^{II}-Schiff base catalytic component is still functional after the grafting procedure and selective towards formation of epoxides. The highest

TONs, in most of the tested substrates, have been provided by **L@MCM-41-Mn^{II}** and **Mn^{II}-L@CMK-3**. The latter catalyst **Mn^{II}-L@CMK-3** is operative for a second use and kinetically very fast demonstrating extremely high TOFs. This fast kinetics of **Mn^{II}-L@CMK-3** in the catalytic epoxidations studied herein is correlated to its no-porosity. Further studies are in progress to elucidate, control and capitalise this important component in heterogeneous catalysis.

Acknowledgment

This research has been co-financed by the European Union (European Social Fund – ESF) and Greek national funds through the Operational Program "Education and Lifelong Learning" of the National Strategic Reference Framework (NSRF) - Research Funding Program: THALIS. Investing in knowledge society through the European Social Fund.

References

- [1] M.G. Clerici, O.A. Kholdeeva, *Liquid Phase Oxidation via Heterogeneous Catalysis: Organic Synthesis and Industrial Applications*, Wiley (2013)
- [2] J. M. Thomas, R. Raja, D.W. Lewis, *Angew. Chem. Int. Ed.* 44 (2005) 6456-6482
- [3] J. M. Thomas, *Design and applications of single-site heterogeneous catalysts: contributions to green chemistry, clean technology and sustainability*. London, UK: Imperial College Press and World Scientific Press (2012)
- [4] D.E. de Vos, M. Dams, B. F. Sols, P. A. Jacobs, *Chem. Rev.* 102 (2002) 3615-3640
- [5] M.H. Valkenberg, W.F. Holderich, *Catal. Rev.* 44 (2002) 321-374
- [6] A. Corma, *Catal. Rev.* 46 (2004) 369-417
- [7] B. S. Lane, K. Burgess, *Chem. Rev.* 103 (2003) 2457-2474
- [8] K. Dimos, P. Stathi, M.A. Karakassides, Y. Deligiannakis, *Microporous and Mesoporous Materials* 126 (2009) 65-71
- [9]] D. Zhao, J. Feng, Q. Huo, N. Melosh, G. H. Fredrickson, B. F. Chmelka, G. D. Stucky, *Science* 279 (1998) 548-552
- [10] R. Ryoo, S.H. Joo, M. Kruk, M. Jaroniec, *Adv Mater* 13 (2001) 677-681
- [11] A. Vinu, T. Mori, K. Ariga, *Sci. Tech. Adv. Mater.* 7 (2006) 753-771
- [12] H.J. Shin, R. Ryoo, M. Kruk, M. Jaroniec, *Chem. Commun.* (2001) 349-350
- [13] M. Kruk, M. Jaroniek, R. Ryoo, S.H. Joo, *J. Phys. Chem. B.* 104 (2000) 7960-7968
- [14] L. Li, Z. H. Zhu, G. Q. Lu, Z.F. Yan, S.Z. Qiao, *Carbon* 45 (2007) 11-20
- [15] Q. Sui, J. Huang, Y. Liu, X. Chang, G. Ji, S. Deng, T. Xie, G. Yu, *J. Environ. Sci.* 23(2) (2011) 177-182.
- [16] Z. Wu, P.A. Webley, D. Zhao, *Langmuir* 26(12) (2010) 10277-10286

- [17] G. Chandrasekar, W.J. Son, W. Ahn, J.Porous. Mater. 16 (2009) 545–551
- [18] F. Lufrano, P. Staiti, Energy Fuels 24 (2010) 3313–3320
- [19] J. Zhang, L.B. Kong, J.J. Cai, Y.C. Luo, L. Kang, Electrochim. Acta 55 (2010) 8067–8073
- [20] H.M.A. Hassan, E.M.Saad, M.S. Soltan, M.A. Betiha, I.S. Butler, S.I. Mostafa, Appl. Catal. A. Gen. 488 (2014) 148-159
- [21] S. Bhunia, S. Koner, Polyhedron 30 (2011) 1857-1864
- [22] M. Masteri-Farahani, F. Farzaneh, M. Ghandi, J. Mol. Catal. A. Chem. 248 (2006) 53-60
- [23] M. Masteri-Farahani, F. Farzaneh, M. Ghandi, Catal. Commun. 8 (2007) 6-10
- [24] S. Tangestaninejad, M. Moghadam, V. Mirkhani, I. Mohammadpoor-Baltork, K. Ghani, Catal. Commun. 10 (2009) 853-858
- [25] M.T. Goldani, A. Mohammad, R.Sandaros, J. Chem.Sci. 126 (2014) 801-805
- [26] X. G. Zhou, X.Q. Yu, J.S. Huang, S.G. Li, L.S. Li, C.M. Che, Chem. Commun. (1999) 1789-1790
- [27] Y. Gang, C. Xing, W. Xiaoli, X. Weihong, X. Nanping, Chinese J. Catal. 34 (2013) 1326-1332
- [28] P. Oliveira, A. Machado, A.M. Ramos, I.M. Fonseca, F.M. Braz. Fernandes, A.M. Botelho do Rego, J. Vital, Catal. Commun. 8 (2007) 1366-1372
- [29] M. Bagherzadeh, M. Zare, M. Amini, T. Salemnoush, S. Akbayrak, S. Ozkar, J. Mol. Catal. A. Chem. 395 (2014) 470-480
- [30] P. Sharma, A. Lazar, A.P. Singh, Appl. Catal. A Gen. 439-440 (2012) 101-110
- [31] H. Gaspar, M. Andrade, C. Pereira, A.M. Pereira, S.L.H. Rebelo, J.P. Araujo, J. Pires, A.P. Carvalho, C. Freire, Catal. Today, 203 (2013) 103-110
- [32] Ch. Vartzouma, E. Evaggellou, Y. Sanakis, N. Hadjiliadis, M. Louloudi, J. Mol. Catal. A 263 (2007) 77-85

- [33] Ag. Stamatis, D. Giasafaki, K.C. Christoforidis, Y. Deligiannakis, M. Louloudi, J. Mol. Catal. A 319 (2010) 58-65
- [34] D. Zois, Ch. Vartzouma, Y. Deligiannakis, N. Hadjiliadis, L. Casella, E. Monzani, M. Louloudi, J. Mol. Catal. A 261 (2007) 306-317
- [35] A. Mavrogiorgou, M. Papastergiou, Y. Deligiannakis, M. Louloudi, J. Mol. Catal. A 393 (2014) 8-17
- [36] E. Seristatidou, A. Mavrogiorgou, I. Konstantinou, M. Louloudi, Y. Deligiannakis, J. Mol. Catal. A (2015)
- [37] Ag. Stamatis, P. Doutsis, Ch. Vartzouma, K.C. Christoforidis, Y. Deligiannakis, M. Louloudi J. Mol. Catal. A 297 (2009) 44-53
- [38] E. Petala, K. Dimos, A. Douvalis, T. Bakas, J. Tucek, R. Zbořil, M.A. Karakassides, Journal of Hazardous Materials 261 (2013) 295-306.
- [39] D. Zhao, Q. Huo, J. Feng, B.F. Chmelka, G.D. Stucky, J. Am. Chem. Soc. 120 (1998) 6024-6036
- [40] S. Jun, S.H. Joo, R. Ryoo, M. Kruk, M. Jaroniec, Z. Liu, T. Ohsuna, O. Terasaki, J. Am. Chem. Soc 122 (2000) 10712-10713
- [41] M. Baikousi, A.B. Bourlinos, A. Douvalis, T. Bakas, D.F. Anagnostopoulos, J. Tuček, K. Šafářová, R. Zboril, M.A. Karakassides, Langmuir 28 (2012), 3918–3930
- [42] G. B. Shul'pin, J. Mol. Catal. A 189 (2002) 39-66
- [43] M. Cardoso, A. R. Silva, B. de Castro, C. Freire, Appl. Catal. A. Gen. 285 (2005) 110–118
- [44] Sravanthi Loganathan, Mayur Tikmani, and Alope K. Ghoshal. Langmuir 2013, 29, 3491–3499.
- [45] Kai-Min Li, Jian-Guo Jiang, Si-Cong Tian, Xue-Jing Chen, and Feng Yan. J. Phys. Chem. C 2014, 118, 2454–2462.
- [46] Ferrari AC, Robertson J. Phys Rev B 2000; 61(20):14095-14107.
- [47] T.W. Kim, I.S. Park, R. Ryoo, Angew. Chem., Int. Ed. 42 (2003) 4375–4379

[48] Fröba, M.; Köhn, R.; Bouffaud, G.; Richard, O.; Van Tendeloo, G. *Chem. Mater.* 1999, 11, 2858–2865.

[49] Huwe, H.; Fröba, M. *Microporous Mesoporous Mater.* 2003, 60, 151–158.

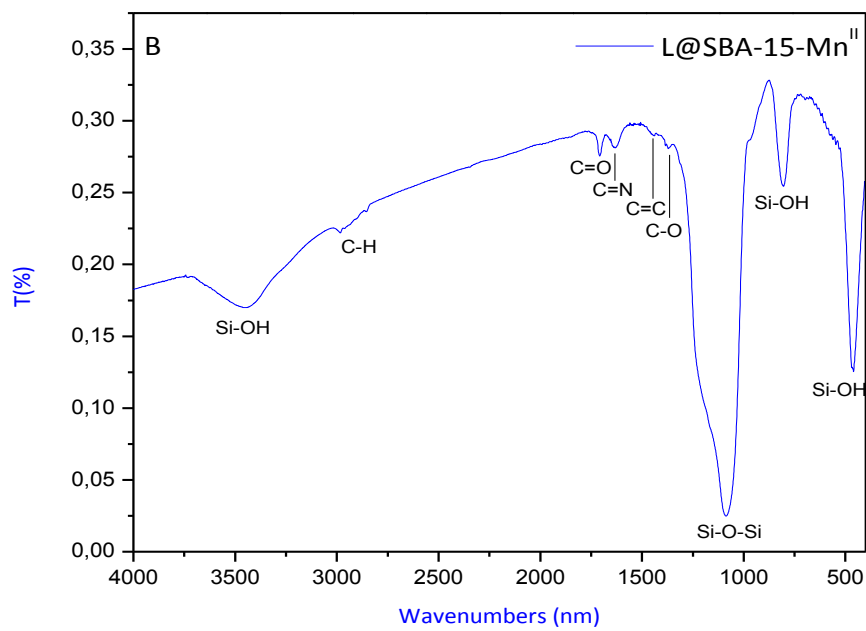
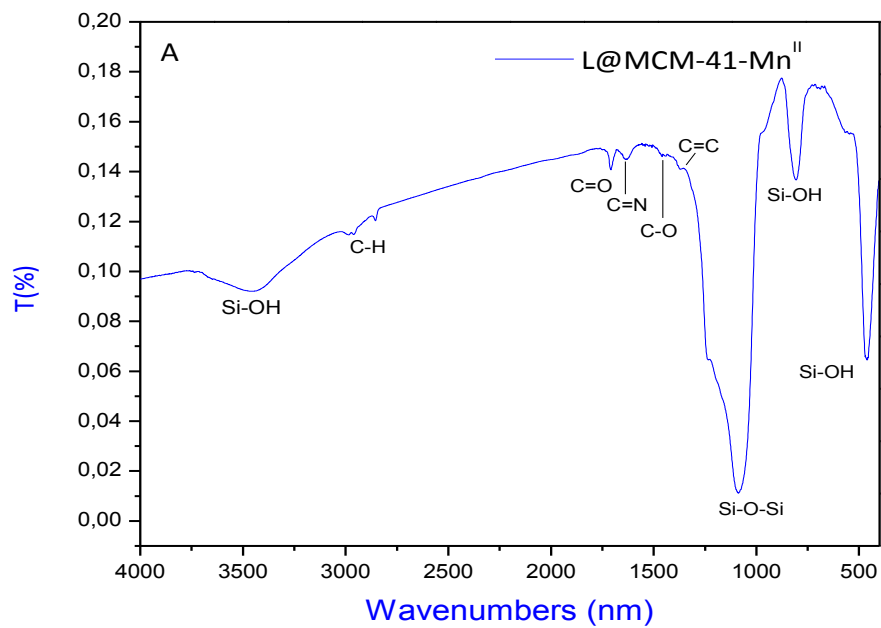
[50] Köhn, R.; Brieler, F.; Fröba, M. *Stud. Surf. Sci. Catal.* 2000, 129, 341–348.

[51] Köhn, R.; Fröba, M. *Catal. Today* 2001, 68, 227–236.

[52] M. Louloudi, Ch. Kolokytha, N. Hadjiliadis, *J. Mol. Catal. A* 180 (2002) 19-24

[53] G. B. Shul'pin, Y. N. Kozlov, L. S. Shul'pina, P. V. Petrovskiy, *Appl. Organometal. Chem.* 24 (2010) 464–472

[54] Ag. Stamatis, Ch. Vartzouma, M. Louloudi, *Catal. Commun.* 12 (2011) 475-479



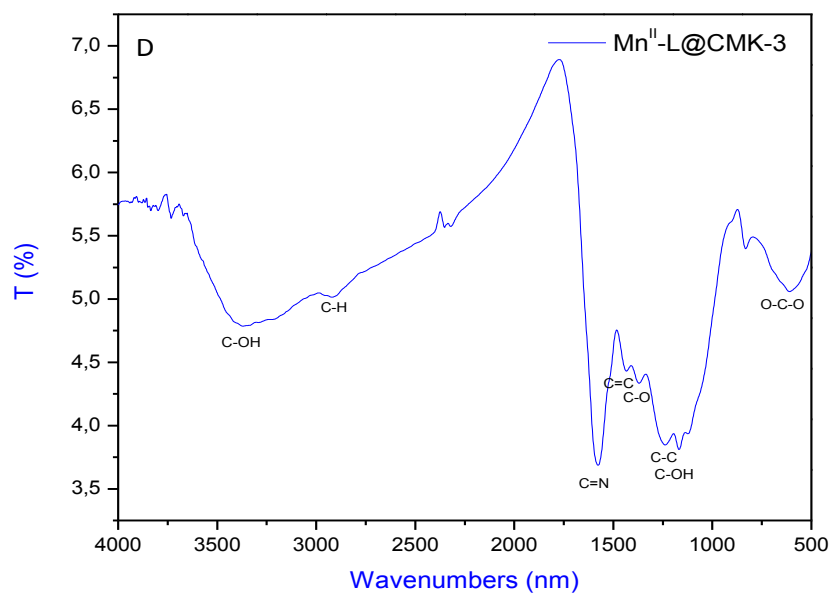
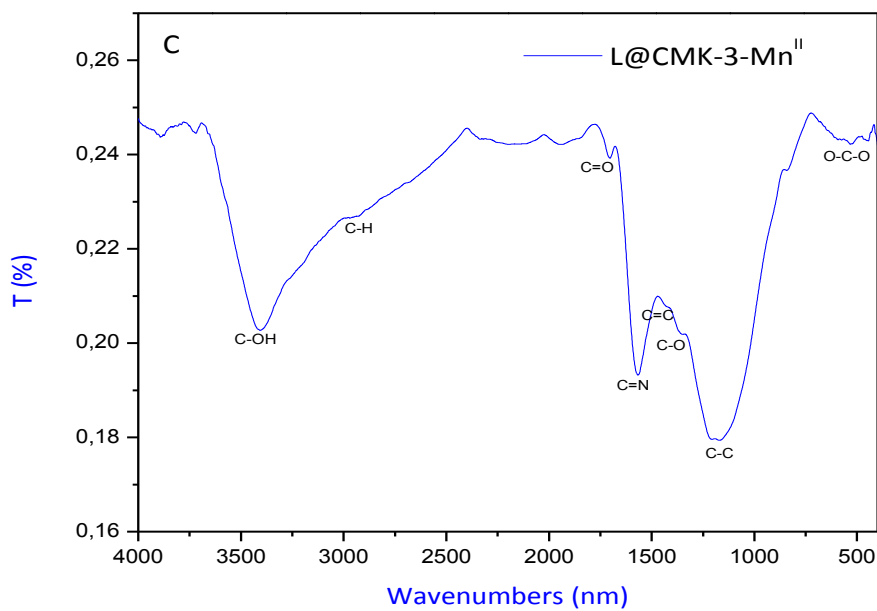


Figure 1 (A-D). FT-IR spectra of, L@MCM-41, L@SBA-15, L@CMK-3-Mn^{II} and Mn^{II}-L@CMK-3 catalysts.

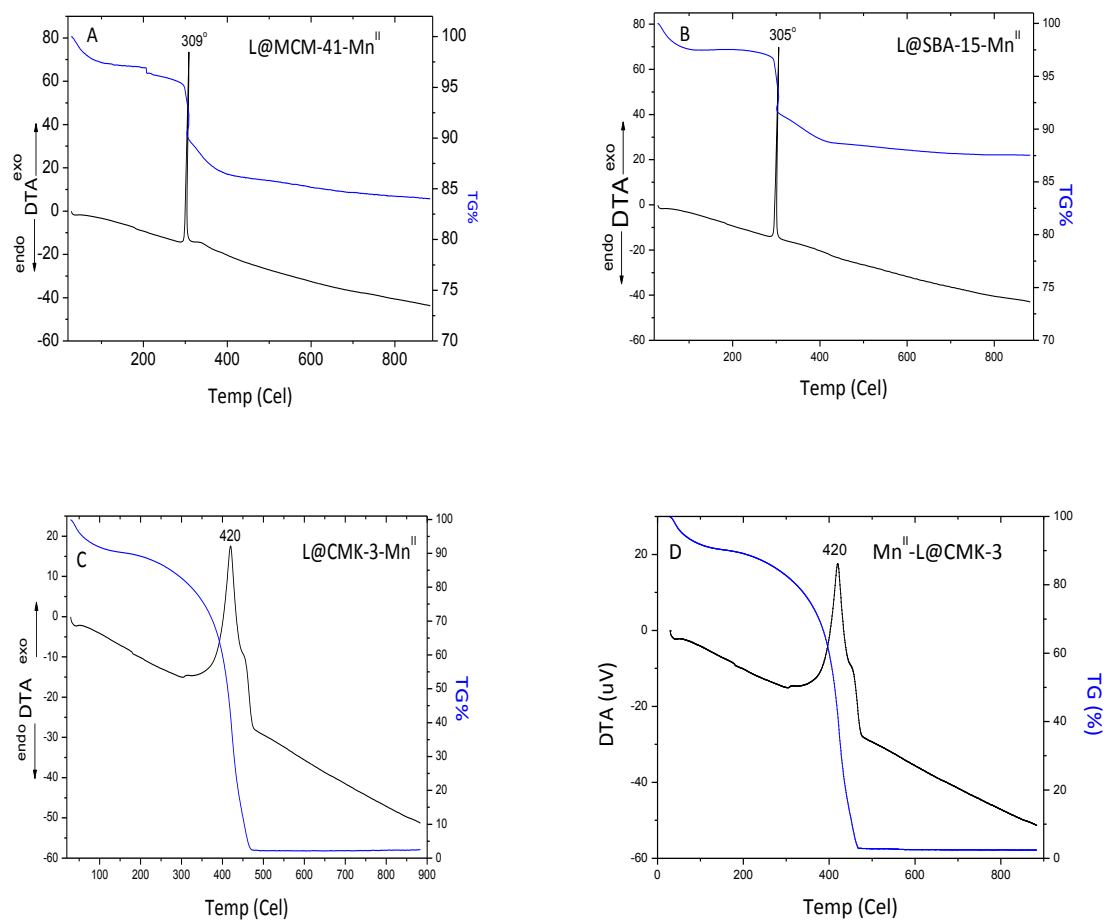


Figure 2 (A-D). The TG-DTA curves of **L@MCM-41-Mn^{II}**, **L@SBA-15-Mn^{II}**, **L@CMK-3-Mn^{II}** and **Mn^{II}-L@CMK-3** catalysts.

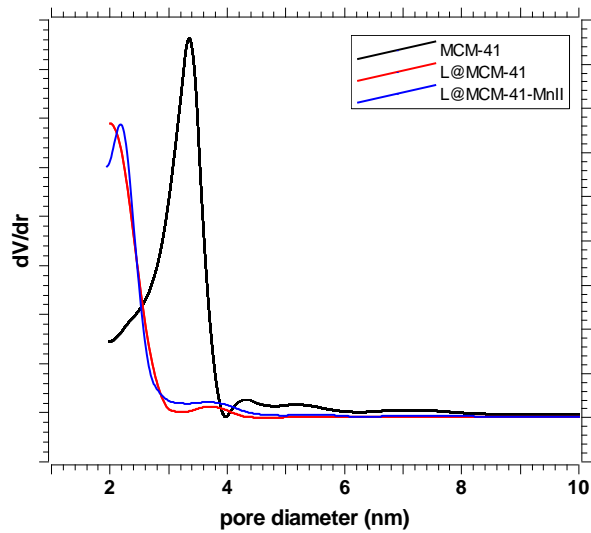
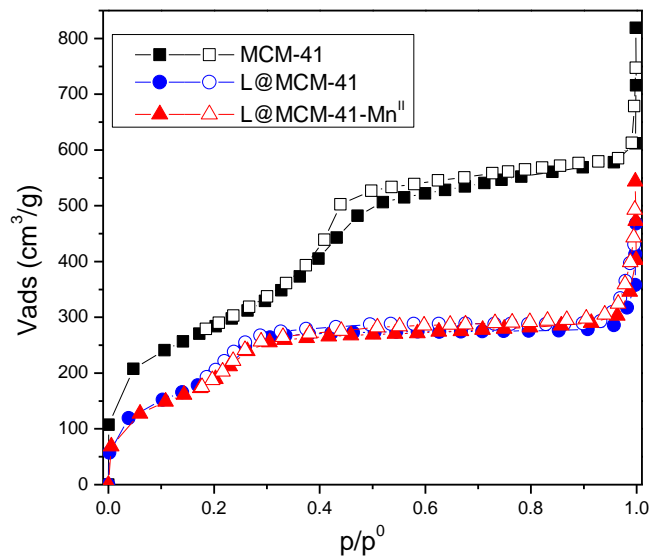


Figure 3. a) N₂ adsorption-desorption isotherms and b) BJH pore size distribution for **MCM-41**, **L@MCM-41** and **L@MCM-41-Mn^{II}**.

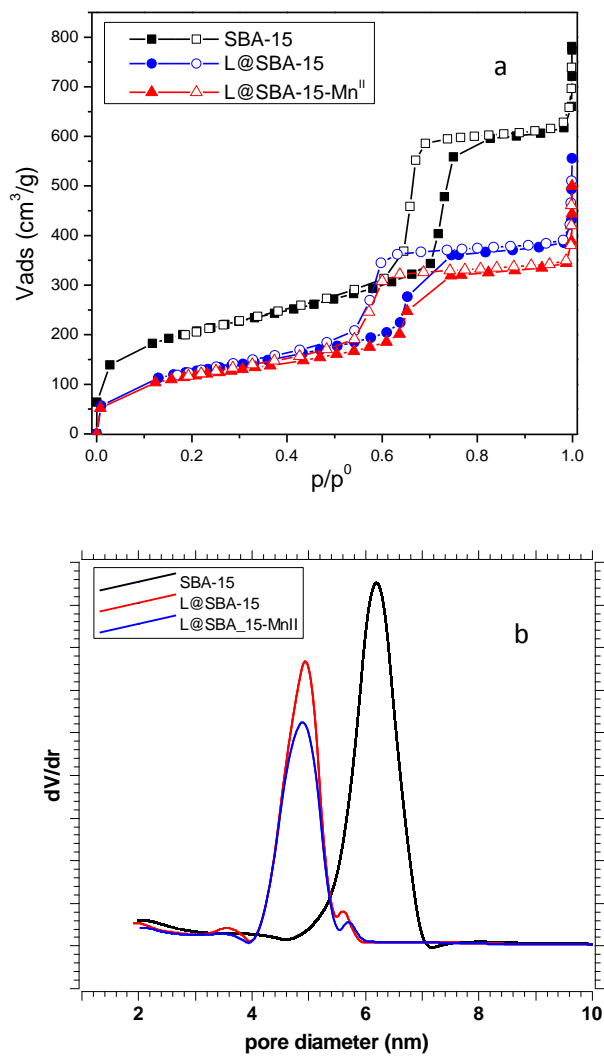


Figure 4. a) N₂ adsorption-desorption isotherms and b) BJH pore size distribution for **SBA-15**, **L@SBA-15** and **L@SBA-15-Mn^{II}**.

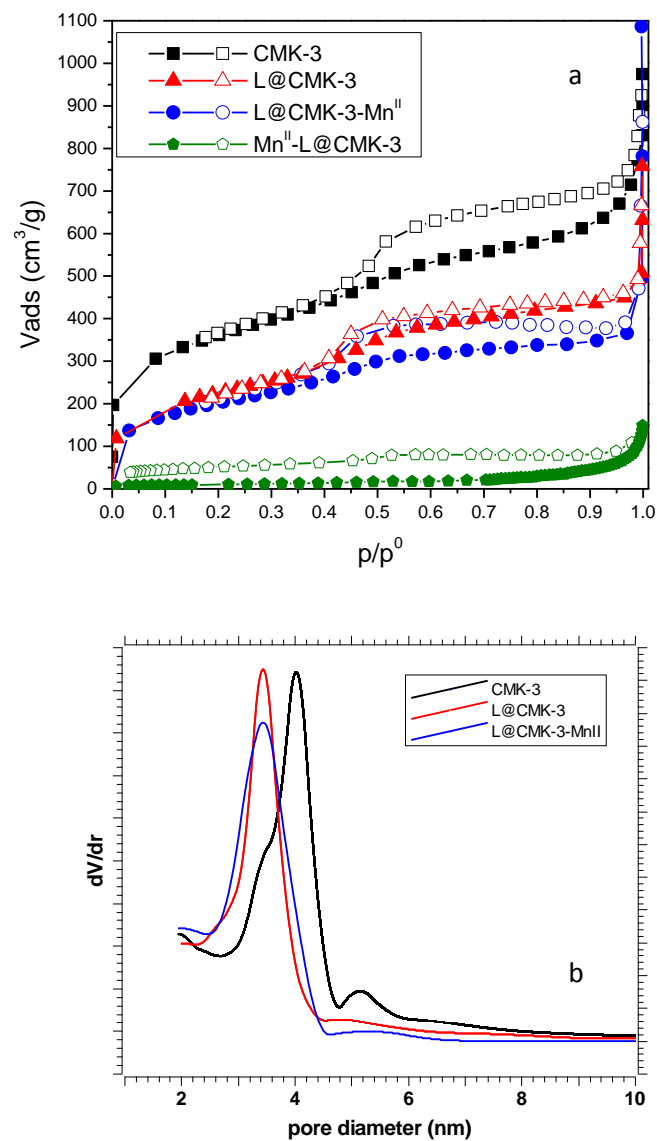


Figure 5. a) N₂ adsorption-desorption isotherms and b) BJH pore size distribution for **CMK-3**, **L@CMK-3**, **L@CMK-3-Mn^{II}** and **Mn^{II}-L@CMK-3**.

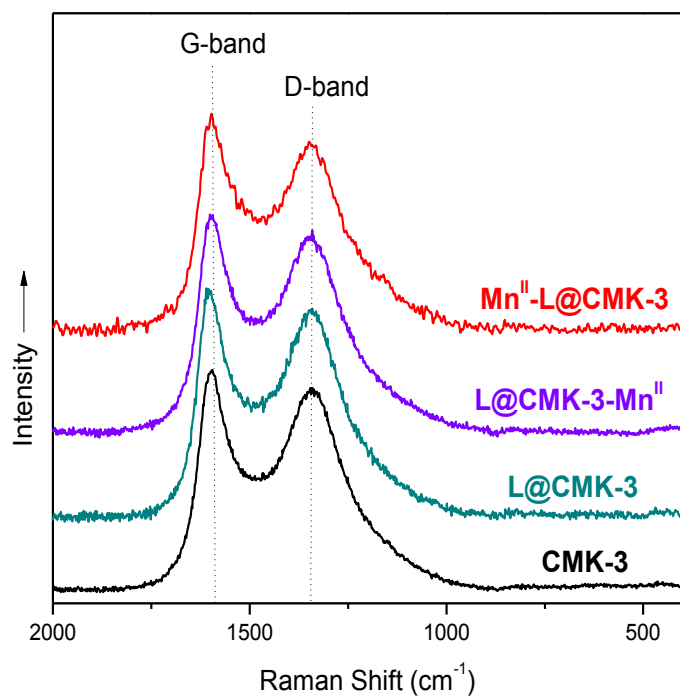
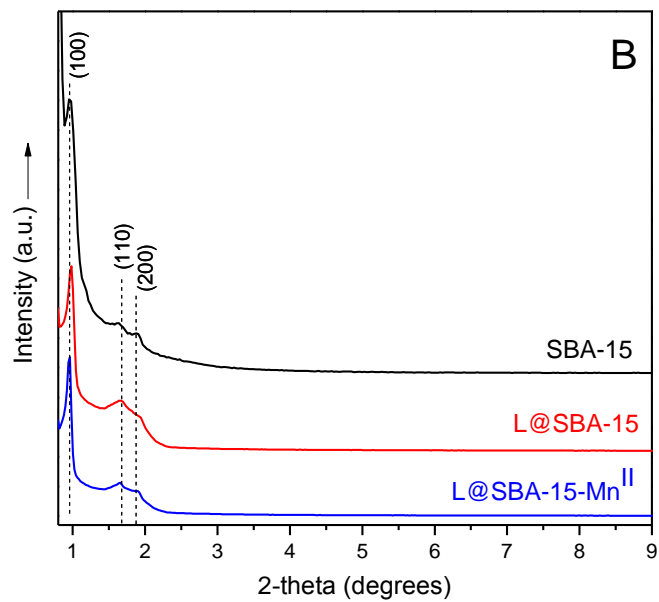
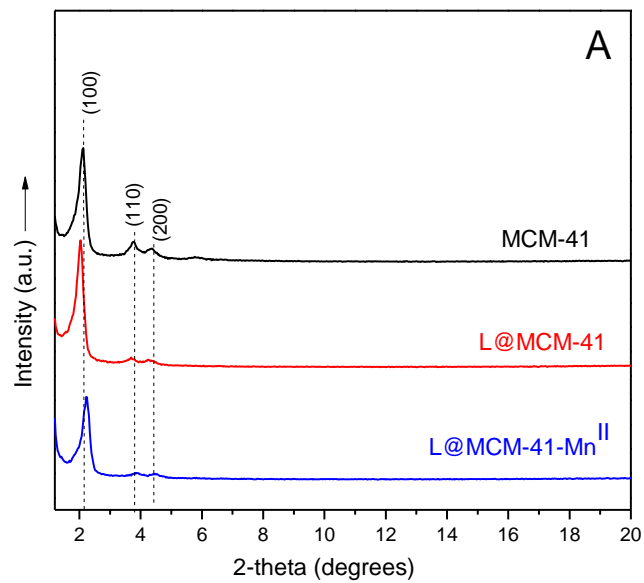


Figure 6. Raman spectra of **CMK-3**, **L@CMK-3**, **L@CMK-3-Mn^{II}** and **Mn^{II}-L@CMK-3** materials.



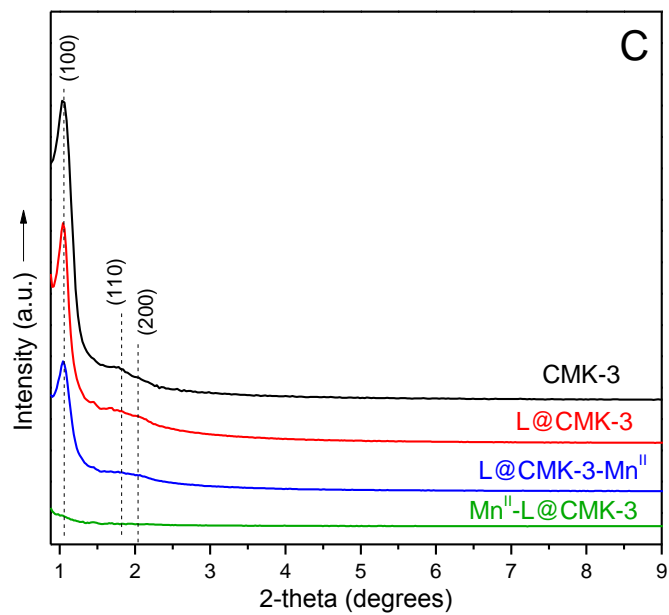


Figure 7 (A,B,C). XRD diffractograms of A) MCM-41- B) SBA-15- and C) CMK-3-based materials.

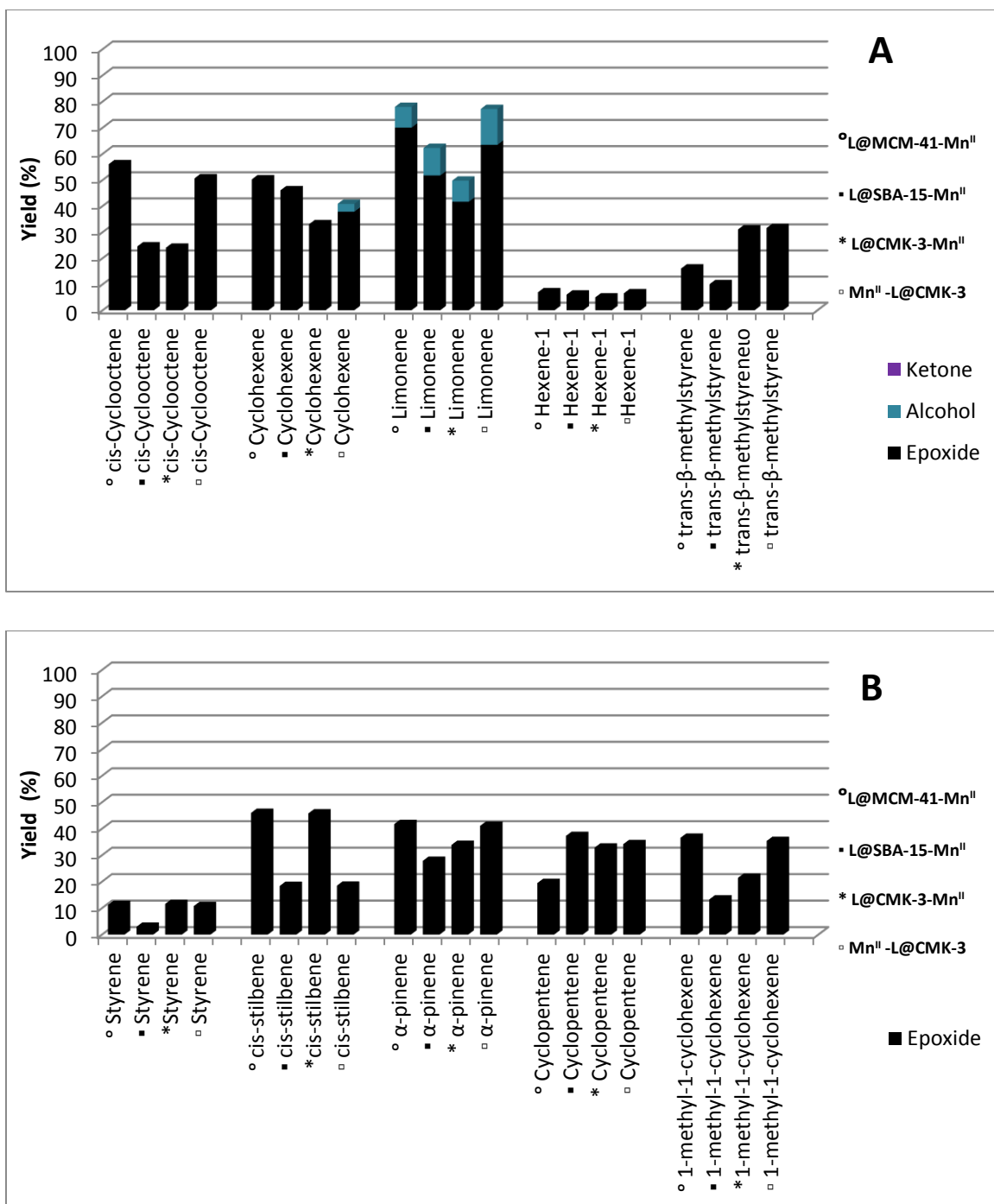


Figure 8 (A and B). Distribution of oxidation products catalyzed by L@MCM-41-Mn^{II}, L@SBA-15-Mn^{II}, L@CMK-3-Mn^{II} and Mn^{II}-L@CMK-3 in the presence of H₂O₂ and CH₃COONH₄. Conditions: [catalyst:H₂O₂ : CH₃COONH₄ : substrate]=[1:2000:1000:1000]; catalyst = 1 μmol in 0.85 ml CH₃COCH₃:CH₃OH (0.45:0.40).

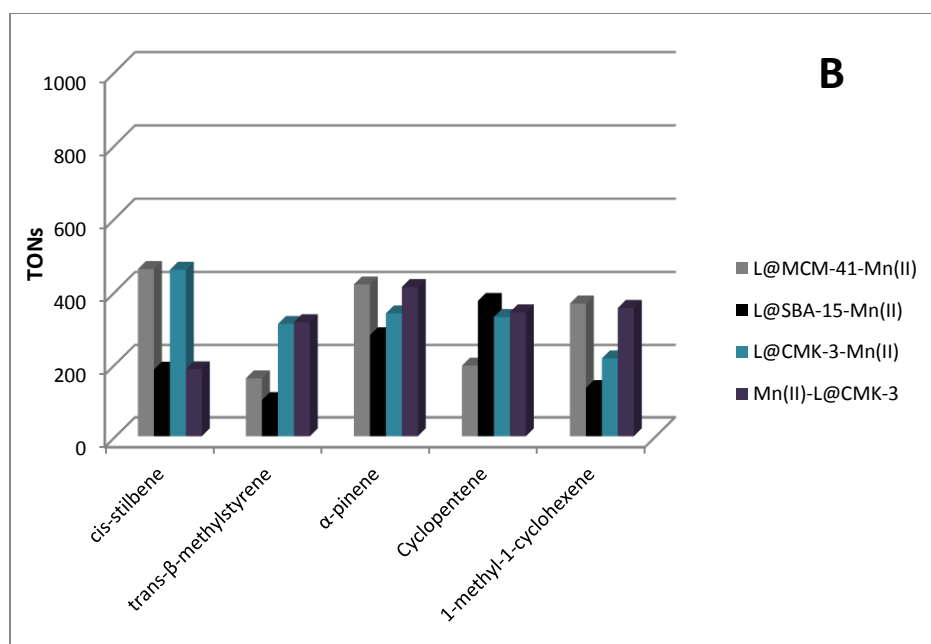
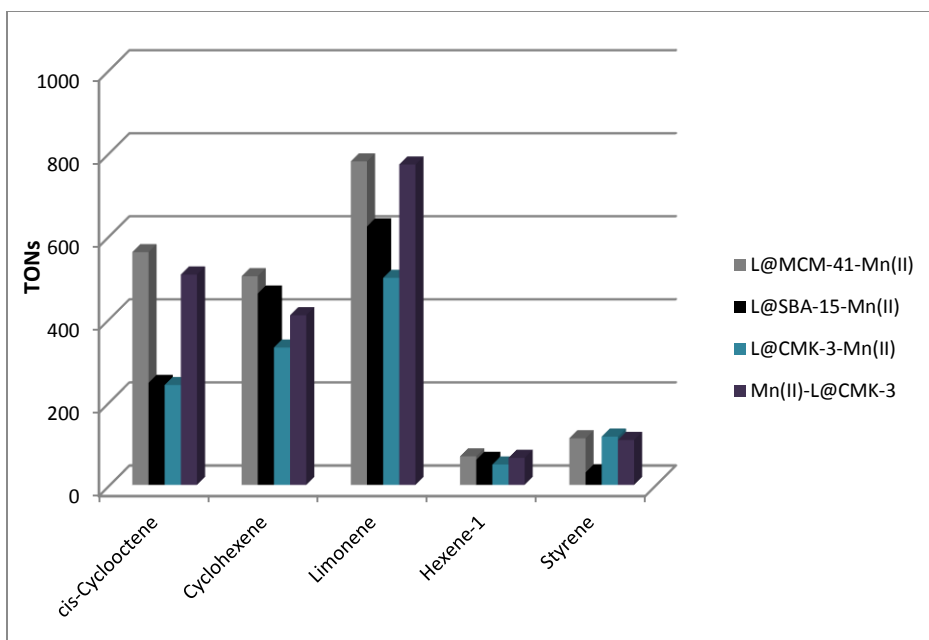


Figure 9 (A and B). Total turnover numbers for alkene epoxidation catalyzed by **L@MCM-41-Mn^{II}**, **L@SBA-15-Mn^{II}**, **L@CMK-3-Mn^{II}** and **Mn^{II}-L@CMK-3** in the presence of H₂O₂. . Conditions: [catalyst:H₂O₂ : CH₃COONH₄ : substrate]=[1:2000:1000:1000]; catalyst = 1 μmol in 0.85 ml CH₃COCH₃:CH₃OH (0.45:0.40).

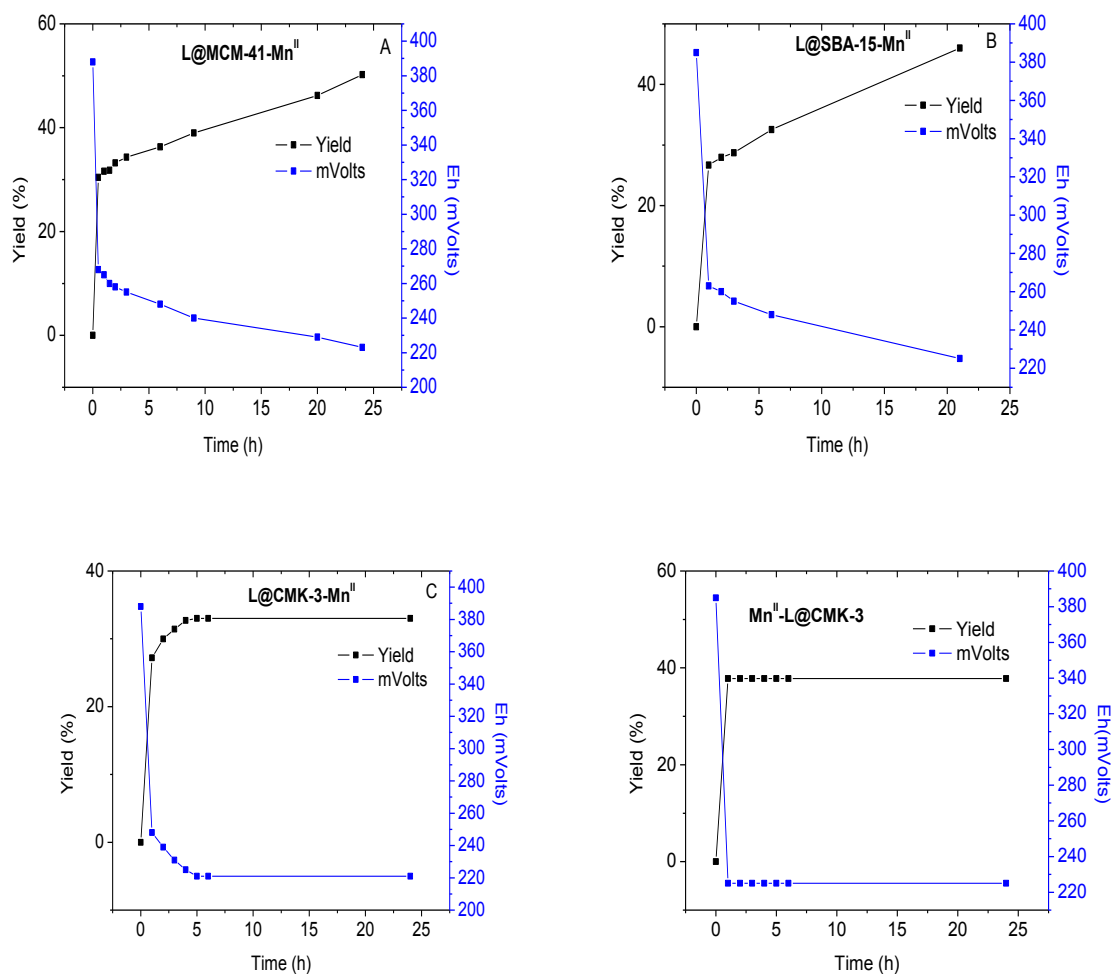


Figure 10 (A-D). Time dependence of cyclohexene epoxidation and solution redox potential for the same reaction catalysed by **L@MCM-41-Mn^{II}**, **L@SBA-15-Mn^{II}**, **L@CMK-3-Mn^{II}** and **Mn^{II}-L@CMK-3**. Conditions: [catalyst:H₂O₂ : CH₃COONH₄ : substrate]=[1:2000:1000:1000]; catalyst = 1 μmol in 0.85 ml CH₃COCH₃:CH₃OH (0.45:0.40).

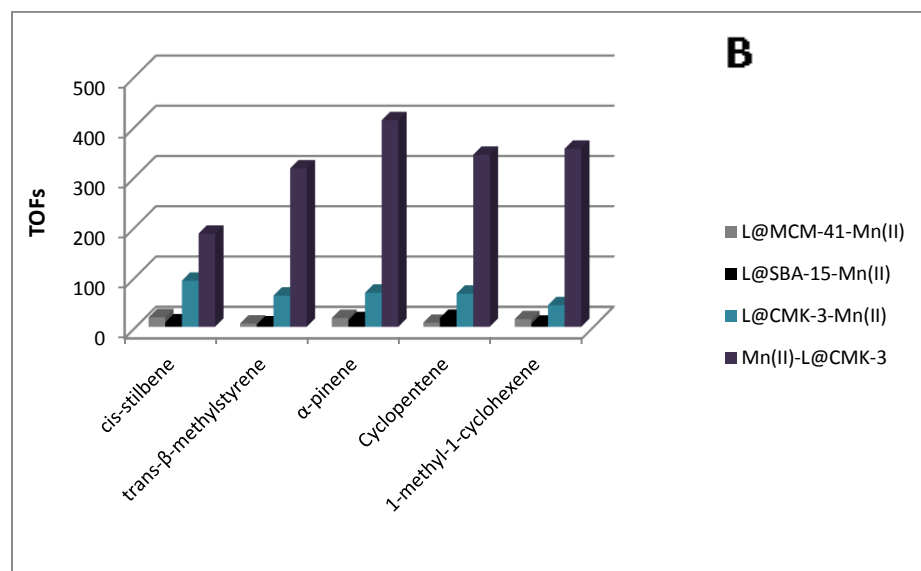
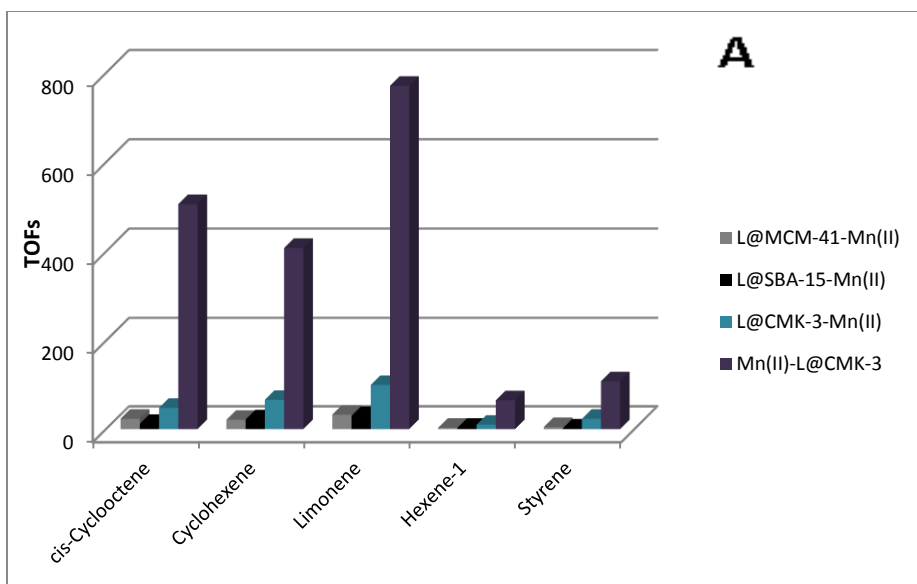


Figure 11 (A and B). TOFs for alkene epoxidation catalyzed by **L@MCM-41-Mn^{II}**, **L@SBA-15-Mn^{II}**, **L@CMK-3-Mn^{II}** and **Mn^{II}-L@CMK-3** in the presence of H₂O₂. . Conditions: [catalyst:H₂O₂ : CH₃COONH₄ : substrate]=[1:2000:1000:1000]; catalyst = 1 μmol in 0.85 ml CH₃COCH₃:CH₃OH (0.45:0.40).

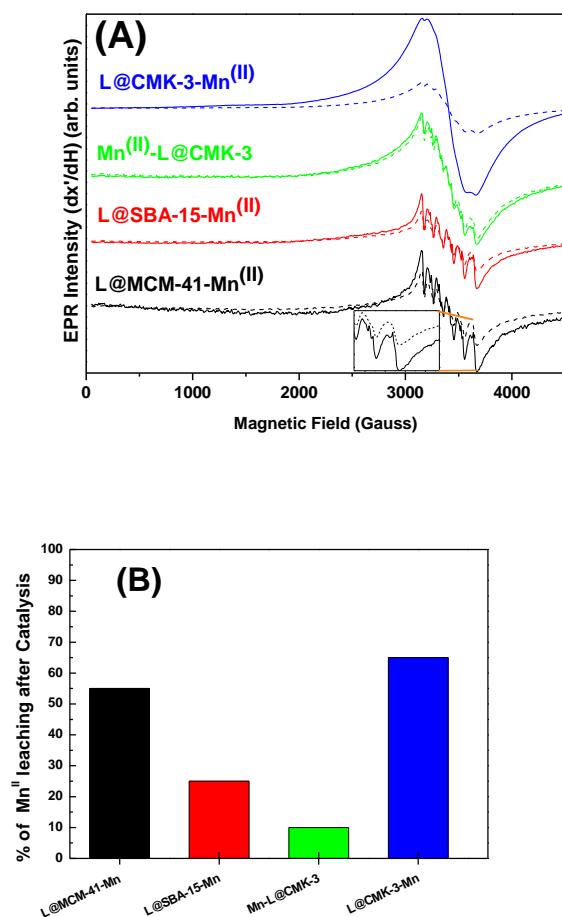
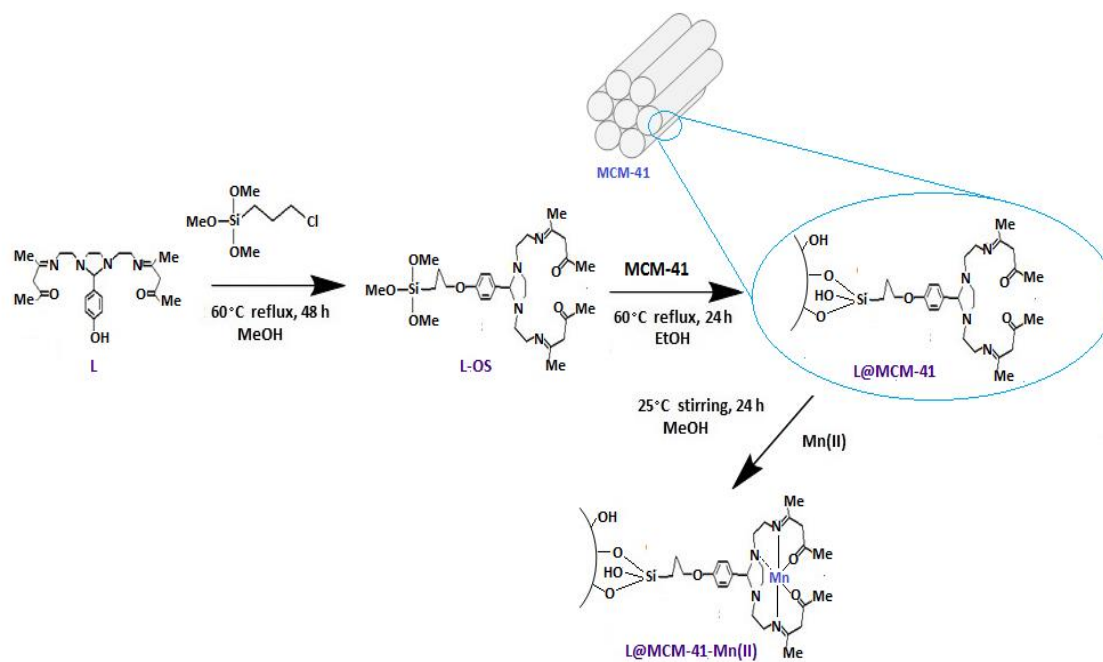
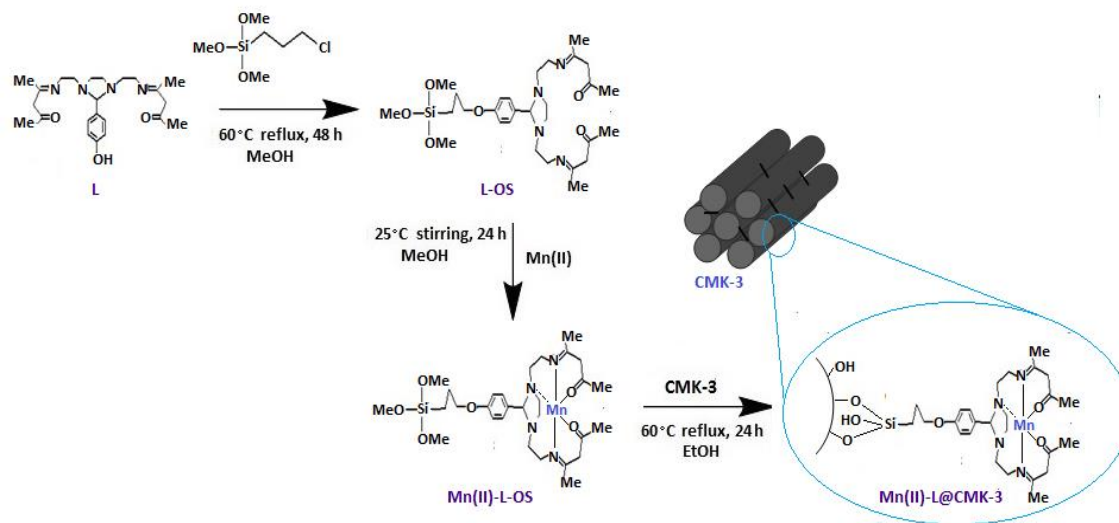


Figure 12. (A): EPR spectra for L@MCM-41-Mn^{II}, L@SBA-15-Mn^{II}, Mn^{II}-L@CMK-3 and L@CMK-3-Mn^{II} catalysts before use (solid lines) and after one catalytic cycle (dotted lines). *Inset*: zoomed part of the spectrum for L@CMK-3-Mn^{II}. The loss of the semi forbidden Mn⁵⁵-hyperfine structure after catalytic use indicates that the Mn^{II}-centers remaining on the material, are not coordinated by the L-ligand. (B): Percent of Mn^{II}-ions after catalysis. *EPR conditions*: temperature 77K, modulation amplitude 10G_{ptp}, microwave power 20mW



Scheme 1. Schematic representation of the $L@MCM-41-Mn^{II}$ heterogeneous catalyst. (In the presence of **SBA-15** or **CMK-3**, the same procedure results to $L@SBA-15-Mn^{II}$ and $L@CMK-3-Mn^{II}$ respectively).



Scheme 2. Schematic representation of the $\text{Mn}^{\text{II}}\text{-L@CMK-3}$ heterogeneous catalyst.

Table 1: Physicochemical features of the prepared materials.

Material	SSA ($\text{m}^2 \text{g}^{-1}$)	Surf. Oxygen groups loading (mmol g^{-1})	Ligand loading (mmol g^{-1})	Mn loading (mmol g^{-1})	Pore diameter (nm)	Pore volume (cm^3/g)
<i>MCM-41</i>	1033				3.3	0.9
<i>L@MCM-41</i>	860		0.26		2.0	0.5
<i>L@MCM-41-Mn^{II}</i>	766		0.28	0.25	2.1	0.5
<i>SBA-15</i>	712				6.2	0.9
<i>L@SBA-15</i>	442		0.24		4.9	0.6
<i>L@SBA-15-Mn^{II}</i>	414		0.20	0.22	4.8	0.5
<i>CMK-3</i>	1260	2.20			4.0	0.9
<i>L@CMK-3</i>	792		0.34		3.4	0.7
<i>L@CMK-3-Mn^{II}</i>	724		0.29	0.26	3.4	0.7
<i>Mn^{II}-L@CMK-3</i>	35		0.32	0.28	-	-

Table 2. Alkene epoxidations catalyzed by single-site Mn^{II}-based catalysts with H₂O₂.^a

Substrates	Products	L@MCM-41-Mn ^{II}			L@SBA-15-Mn ^{II}			L@CMK-3-Mn ^{II}			Mn ^{II} -L@CMK-3		
		Yield (%) ^b	TON ^c	TOF (h ⁻¹) ^d	Yield (%) ^b	TON	TOF (h ⁻¹) ^d	Yield (%) ^b	TON	TOF (h ⁻¹) ^d	Yield (%) ^b	TON	TOF (h ⁻¹) ^d
cis-Cyclooctene	cis-epoxide	56.0	560	23.3	24.5	245	11.6	24.0	240	48	50.6	506	506
Cyclohexene	cis-epoxide 2-Cyclohexenol	50.2	502	20.9	46.0	460	21.9	33.0	330	66	37.8 3.0	408	408
Limonene ^e	1,2-epoxide	70.0	779	32.5	51.7	622	29.6	41.6	498	99.6	63.4	771	771
	(cis/trans)-alcohol	(39.0/31.0)			(29.1/22.6)			(23.2/18.5)			(35.0/28.4)		
		7.9			10.5			8.1			13.7		
Hexene-1	cis-epoxide	6.9	69	2.9	6.0	60	2.9	4.9	49	9.8	6.5	65	
Trans- β -methylstyrene	cis-epoxide	16.0	160	6.6	10.0	100	4.8	31.0	310	6.6	31.5	315	315
Styrene	Epoxide	11.2	112	4.6	3.0	30	1.4	11.6	116	23.2	10.8	108	108
cis-Stilbene	cis-epoxide	46.0	460	19.1	18.4	184	8.8	45.8	458	91.6	18.5	185	185
α -Pinene	Epoxide	41.8	418	17.4	27.9	279	13.3	33.9	339	67.8	41.1	411	411
Cyclopentene	Epoxide	19.5	195	8.0	37.3	373	17.8	32.9	329	65.8	34.2	342	342
1-methyl-1cyclohexene	Epoxide	36.6	366	15.2	13.3	133	6.3	21.5	215	43.0	35.4	354	354

^a Conditions- ratio of catalyst : H₂O₂ : CH₃COONH₄ : substrate=1:2000:1000:1000; equivalent of catalyst = 1 μ mol in 0.85 ml CH₃COCH₃:CH₃OH (0.45:0.40). ^b Yields based on starting substrate and products formed. The mass balance is 98-100%. ^cTON :total turnover number, moles of products formed per mole of catalyst. ^d TOF : turnover frequency which is calculated by the expression [epoxide]/[catalyst] x time (h⁻¹). ^e Limonene 1,2-oxide was found as a mixture of cis- and trans- isomers.

Table 3. Recyclability of the single-site heterogeneous Mn^{II}-catalysts.^a

	<i>Cyclooctene epoxide yield (%)</i>			
	L@MCM-41-Mn^{II}	L@SBA-15-Mn^{II}	L@CMK-3-Mn^{II}	Mn^{II}-L@CMK-3
1st use	56.2	24.5	24.0	50.6
2nd use	0.5	0.4	10.0	21.5
3rd use	-	-	0.5	0.6

^a Conditions- [catalyst : H₂O₂ : CH₃COONH₄ : substrate]=[1:2000:1000:1000]; catalyst = 1 μmol in 0.85 ml CH₃COCH₃:CH₃OH (0.45:0.40).